Truchet-tile structure of a topologically aperiodic metal–organic framework

Emily G. Meekel,[1] Ella M. Schmidt,[1,2] Lisa J. Cameron,[3] A. David Dharma,[3] Hunter J. Windsor,[3] Samuel G. Duyker,[3,4] Arianna Minelli,[1] Tom Pope,[5] Giovanni Orazio Lepore,[6] Ben Slater,[5] Cameron J. Kepert[3,*] and Andrew L. Goodwin[1,*]

[1]*Inorganic Chemistry Laboratory, University of Oxford, Oxford OX1 3QR, UK*

[2]*Fachbereich Geowissenschaften, Universität Bremen, D-28359 Bremen, Germany*

[3]*School of Chemistry, University of Sydney, NSW 2006, Australia*

[4]*Sydney Analytical, Core Research Facilities, University of Sydney, NSW 2006, Australia*

[5]*Department of Chemistry, University College London, London WC1H 0AJ, UK*

[6]*Earth Sciences Department, University of Florence, Florence 50121, Italy*

When tiles decorated to lower their symmetry are joined together, they can form aperiodic and labyrinthine patterns. Such Truchet tilings offer an efficient mechanism of visual data storage related to that used in barcodes and QR codes. We show that the crystalline metal–organic framework $[OZn_4][1,3\text{-benzenedicarboxylate}]_3$ (TRUMOF-1) is an atomic-scale realization of a complex three-dimensional Truchet tiling. Its crystal structure consists of a periodically-arranged assembly of identical zinc-containing clusters connected uniformly in a well-defined but disordered fashion to give a topologically aperiodic microporous network. We suggest that this unusual structure emerges as a consequence of geometric frustration in the chemical building units from which it is assembled.

In 1704, Sébastian Truchet described a variety of visually appealing patterns generated by a single square tile painted differently either side of its diagonal (*1*). Truchet always arranged his tiles on the same square lattice,

but obtained different patterns by varying the orientations of each tile. Truchet tilings have been generalized to encompass any periodic covering of space (partial or complete) with one or more tiles that have been decorated to reduce their symmetry (*2*). Breaking color-inversion symmetry, for example, gives barcodes and QR codes as simple Truchet tilings in one and two dimensions, respectively: each strip or pixel encodes a binary state that is exploited in their application as machine-readable information stores (Fig. 1A). More complex Truchet tilings store information in aperiodic patterns of loops and networks in two or three dimensions (Fig. 1B,C) (*3*).

Because the solid-state structures of many crystalline materials can be related to periodic tilings of three-dimensional space (*4*), we explored the possibility of realizing an atomic-scale Truchet tiling in metal–organic frameworks (MOFs), given that their structures can be controlled through judicious selection of the nodes and linkers from which they are assembled (*5*). In the canonical system MOF-5 $[OZn_4][1,4\text{-bdc}]_3$, the combination of OZn_4 as the octahedrally-coordinating node and bdc, benzenedicarboxylate, as the connecting linker generates a structure with the simple cubic topology (*6*). This structure can be mapped to the tiling of space by cubes (*7*).

Greater complexity can be introduced into MOFs by lowering the symmetry of their building blocks (*8*, *9*), and we synthesized a new derivative of MOF-5 in which the linear 1,4-bdc linker was replaced by its bent 1,3-bdc analog. The crystalline material we obtained, which we call TRUMOF-1, produced an x-ray diffraction (XRD) pattern that included both conventional Bragg diffraction reflections and very weak diffuse scattering. Because the underlying chemistries of TRUMOF-1 and MOF-5 were so similar, we anticipated that the composition of TRUMOF-1 should be $[OZn_4][1,3\text{-bdc}]_3$. Structure solution from the Bragg component (sensitive only to the configurational average) gave the result shown in Fig. 2A: $[OZn_4]$ clusters were positioned at the corners and face-centers of the $F\bar{4}3m$ cubic unit cell and connected by what appeared to be trigonally-symmetric linker molecules that were only partly occupied. Distinguishable in the Fourier maps at

the linker sites are benzene C atoms and carboxylate C/O atoms, the occupancies of which refined to values of 0.70(4) and 0.46(3), respectively; these occupancies implied a crystal composition of $[OZn_4][1,3\text{-bdc}]_{2.8(2)}$ and are near the values (0.75 and 0.5) expected for the idealized composition $[OZn_4][1,3\text{-bdc}]_3$. The configurational averages of Truchet tilings necessarily contain features with partial occupancies (Fig. 1).

We were able to synthesize TRUMOF-1 in bulk, and powder samples produced XRD patterns entirely consistent with our single-crystal measurements (Fig. S6). The framework pores of as-synthesized samples contained solvent, which could be exchanged with other solvents or removed by heating under vacuum. The empty framework adsorbed a range of gases (including CO_2) and had a Brunauer-Emmett-Teller (BET) surface area of 765 $m^2\ g^{-1}$ (Fig. S12). Its thermal stability was similar to that of MOF-5 but its adsorption enthalpies were about twice as large (Figs. S4, S13), indicative of the presence of smaller pores. In all these various respects, TRUMOF-1 behaves as a conventional MOF (*10*).

We interpreted the average crystal structure of TRUMOF-1 by first considering the partially-occupied ligand site. ^1H and ^{13}C nuclear magnetic resonance (NMR) spectra of acid-digested TRUMOF-1 samples revealed the only bridging ligand to be 1,3-bdc (Fig. S2), so the crystallographic model must represent an average over three equally-populated orientations of the 1,3-bdc linker (Fig. 2B). The emergence of an apparently threefold-symmetric ligand resulted from the crystallographic site having higher point symmetry than the linker itself. To give the chemically sensible stoichiometry $[OZn_4][1,3\text{-bdc}]_3$, the site must also be vacant with 25% probability; note that this value was consistent with the observed site occupancies.

In contrast, the OZn_4 cluster appeared ordered and fully occupied. The cluster was surrounded by 12 carboxylate anion sites, each occupied with 50% probability. Zinc K-edge extended x-ray fine structure (EXAFS) measurements showed the Zn coordination environment to be essentially identical to that in the octahedrally-coordinated OZn_4 clusters of MOF-5 (*11*) (Fig. S11). We incorporated this finding into the

crystallographic model in terms of a configurational average over 24 symmetry-related octahedral-coordination decorations of the cluster (Fig. 2C). Again, each cluster decoration had lower point symmetry than the crystallographic site on which the cluster sat (the carboxylate positions broke ideal octahedral symmetry, Fig. S15). On purely geometric grounds, the various partial site occupancies should be strongly correlated because the orientation of a given cluster decoration placed strong constraints on which neighboring 1,3-bdc linkers were present and in which possible orientations they could lie (*12*, *13*).

Both local symmetry-lowering and orientational matching rules allowed us to map the structure to a three-dimensional Truchet tiling, and we tested this model both computationally and experimentally. To obtain the underlying tiling, we used a Voronoi decomposition of the crystal structure based on the average cluster and ligand positions. The two tile shapes so produced—a cube and a trigonal bipyramid—filled three-dimensional space when placed on the TRUMOF-1 cluster and ligand sites, respectively. The Truchet decorations are given by the symmetry-lowering implied by 1,3-bdc occupancies in the TRUMOF-1 crystal structure (Fig. 2D).

For example, each cube is decorated by a pseudo-octahedral arrangement of rods that capture the arrangement of carboxylate substituents around each OZn_4 cluster. Likewise, three quarters of the trigonal bipyramids were decorated by an arc that reflected the bent linking geometry of a 1,3-bdc molecule. The remaining quarter of the trigonal bipyramidal tiles were left undecorated. Four triangular bipyramids packed together to form a cube. Any combination of orientations of these different tiles—alternating on their respective sites—that produced a connected network then would relate to a chemically-sensible model of 1,3-bdc-linked OZn_4 clusters in which each cluster was octahedrally coordinated by six 1,3-bdc linkers and each 1,3-bdc linker connected exactly two clusters (Fig. 2E). There are infinitely many such networks.

To test whether this Truchet-tile description of TRUMOF-1 is physically reasonable, we performed a series of ab initio density functional theory (DFT) calculations. Our approach was to calculate the geometry and cell

optimized 0 K energies of periodic realizations ("approximants") (*14*) of the system with increasingly large unit cells so as to understand the underlying energetic landscape. There were only three symmetry-distinct 1 × 1 × 1 approximants—that is, with unit cells commensurate with the (∼15 Å)^3 cell of the average structure. Each relaxed to give a sensible structure, like that shown in Fig. 2E, with ten distinct realizations giving equilibrium energies within a few kilojoules per mole of Zn of one another.

The number of possible configurations grew very quickly with system size. For the 2 × 2 × 2 case (32 formula units; 1696 atoms), there were too many possibilities to enumerate, so we focused on 20 representative realizations. These larger configurations spanned a wider range of energies and had more open structures (Fig. 3A); the range of unit-cell volumes we observed was characteristic of flexible MOF structures (*15*). Because the enthalpic differences amongst these periodic TRUMOF-1 approximants were commensurate with solvent binding enthalpies in zinc carboxylate MOFs (such as MOF-5) (*16*, *17*), we expected that guest inclusion would reduce the spread of energies in practice because loading would be higher in the less dense realizations. Hence, we concluded that the configurational landscape accessible to TRUMOF-1 spanning different Truchet-tile arrangements involved many thermally accessible minima. This finding helped to explain why synthesis at ∼400 K generated a disordered rather than ordered configuration. Aperiodic networks would also be favored on entropic grounds.

The experimental measurement with greatest sensitivity to structural disorder and its correlation in crystalline materials is single-crystal diffuse scattering (*18*). All disordered materials give rise to diffuse scattering, but the presence of structure in this scattering implies non-random disorder and its form can be diagnostic of specific correlations governing local structure (*19*, *20*). The experimental x-ray diffuse scattering pattern of TRUMOF-1 was dominated by transverse-polarized diagonal features characteristic of correlated displacements (Fig. 3B) (*21*). Because we did not find any strong temperature-dependence to the scattering, this contribution could be attributed predominantly to static displacements, rather than to thermal effects. The

corresponding three-dimensional difference pair-distribution function (3D-ΔPDF) captured the real-space correlations from which the diffuse scattering arose (Fig. 3C) (*22*). The diffuse scattering and 3D-ΔPDF calculated from our larger DFT-relaxed configurations closely matched experiment (Fig. 3C,D), indicating that the Truchet-tile model from which these configurations are generated captured the fundamental nature of correlated disorder in TRUMOF-1. The subtle differences were attributed to the finite size of our DFT model—hence sharpness of features in reciprocal space—and the role of dynamical effects— most obviously affecting low-|**r**| features in the 3D-ΔPDF. We anticipate even better agreement for larger approximants (were they computationally accessible), which would more closely approximate the aperiodic limit. A more detailed discussion of the sensitivity of the diffuse scattering to different aspects of our Truchet-tile model is given in the Supplementary Text.

As a further check against experiment, we show in Fig. 3D that the distribution of atomic positions determined from configurational averaging over our DFT configurations was consistent with the anisotropic displacement parameters determined in our single-crystal XRD refinements. Our model indicated that static disorder contributed ~ 0.1 $Å^2$ to atomic mean-squared displacements in the $F\bar{4}3m$ average structure model. A similar value was obtained by extrapolating to 0 K the experimental displacement parameters measured between 100 and 350 K (Fig. S18). Hence, our Truchet-tile model rationalizes at once both average and local structure measurements of the structure of TRUMOF-1.

The topology of TRUMOF-1 is unusual in a number of respects. The MOF network is a fully 6-connected net with nodes arranged on a periodic lattice (as in MOF-5) but its connectivity is aperiodic (in contrast to MOF-5). No two crystals would have the same network connectivity—that is, they store different information—despite sharing the same statistical properties. The system is intermediate to conventional crystalline MOFs and amorphous MOF derivatives with continuous random network structures (*23*, *24*). The topological aperiodicity of TRUMOF-1 may be important because it translates into a disordered pore network with

specific characteristics (*25*). We found that guest molecules were sensitive to this aperiodicity because loading TRUMOF-1 crystals with I_2 enhanced the x-ray diffuse scattering contrast (Fig. S9). A representative pore structure, extracted from one of our DFT configurations, is illustrated in Fig. 4. The complex transport pathways we observed were qualitatively similar to those in gels (*26*) and granular porous media (*27*) and so may be useful in separations. We found good consistency between experimental adsorption behavior and that calculated from grand canonical Monte Carlo simulations based on our structural model; as anticipated, the smaller pore dimensions relative to MOF-5 reflect the stronger adsorption enthalpies of TRUMOF-1 (Fig. S14).

There is no reason to expect that TRUMOF-1 should be the unique MOF with a Truchet-tile structure. Because every conventional periodic tiling can be modified to give Truchet tilings, suitable symmetry-lowering of inorganic and organic building units should allow targeted synthesis of alternative Truchet MOFs. Indeed, the structures of some previously-described MOFs (*28*) and related systems (*29*) with partially-occupied and/or complex structures might be reinterpretable as Truchet tilings. We note that TRUMOF-1 was assembled from an inorganic component predisposed to forming extended network structures (*30*) and an organic component usually used in the formation of discrete molecular cages (*31*). The concept of geometrically frustrating the competing structure-directing effects of two synthons to drive a complex state may generalize beyond this particular system (*32*). The discovery of a crystalline Truchet-tile material allows experimental investigation of the impact of aperiodic connectivity on collective materials properties. Aperiodicity could frustrate elastic instabilities (*33*) or dampen long-wavelength acoustic phonons—as occurs in superlattice heterostructures (*34*) and as required for optimizing thermoelectric response (*35*). As such, Truchet-tile-inspired systems may provide a useful avenue for the design of a variety of functional systems.

References

1. Truchet, S. Mémoir sur les combinasions. Mem. Acad. R. Sci. Paris 363–372 (1704).

2. Smith, C. S. The tiling patterns of Sebastien Truchet and the topology of structural hierarchy. *Leonardo* **20**, 373–385 (1987).

3. Browne, C. Truchet curves and surfaces. *Comput. Graph.* **32**, 268–281 (2008).

4. Blatov, V. A., Delgado-Friedrichs, O., O'Keeffe, M. & Proserpio, D. M. Three-periodic nets and tilings: natural tilings for nets. *Acta Cryst. A***63**, 418–425 (2007).

5. Delgado-Friedrichs, O., O'Keeffe, M. & Yaghi, O. M. Taxonomy of periodic nets and the design of materials. *Phys. Chem. Chem. Phys.* **9**, 1035–1043 (2007).

6. Li, H., Eddaoudi, M., O'Keeffe, M. & Yaghi, O. M. Design and synthesis of an exceptionally stable and highly porous metal-organic framework. *Nature* **402**, 276–279 (1999).

7. O'Keeffe, M. Nets, tiles, and metal-organic frameworks. *APL Mater.* **2**, 124106 (2014).

8. Guillerm, V. & Maspoch, D. Geometry mismatch and reticular chemistry: Strategies to assemble metal–organic frameworks with non-default topologies. *J. Am. Chem. Soc.* **141**, 16517–16538 (2019).

9. Meekel, E. G. & Goodwin, A. L. Correlated disorder in metal–organic frameworks. *CrystEngComm* **23**, 2915–2922 (2021).

10. Eddaoudi, M., Li, H. & Yaghi, O. M. Highly porous and stable metal-organic frameworks: Structure, design and sorption properties. *J. Am. Chem. Soc.* **122**, 1391–1397 (2000).

11. Hafizovic, J. et al. The inconsistency in adsorption properties and powder XRD data of MOF- 5 is rationalized by framework interpenetration and the presence of organic and inorganic species in the nanocavities. *J. Am. Chem. Soc.* **129**, 3612–3620 (2007).

12. Simonov, A. & Goodwin, A. L. Designing disorder into crystalline materials. *Nat. Rev. Chem.* **4**, 657–673 (2020).

13. Ehrling, S. et al. Adaptive response of a metal–organic framework through reversible disorder–disorder transitions. *Nat. Chem.* **13**, 568–574 (2021).

14. Thygesen, P. M. M. et al. Orbital dimer model for the spin-glass state in $Y_2Mo_2O_7$. *Phys. Rev. Lett.* **118**,

067201 (2017).

15. Krause, S. et al. A pressure-amplifying framework material with negative gas adsorption transitions. *Nature* **532**, 348–352 (2016).

16. Hughes, J. T. & Navrotsky, A. MOF-5: Enthalpy of formation and energy landscape of porous materials. *J. Am. Chem. Soc.* **133**, 9184–9187 (2011).

17. Brozek, C. K. et al. Dynamic DMF binding in MOF-5 enables the formation of metastable cobalt-substituted MOF-5 analogues. *ACS Cent. Sci.* **1**, 252–260 (2015).

18. Welberry, T. R. Diffuse X-ray scattering and models of disorder. *Rep. Prog. Phys.* **48**, 1543–1593 (1985).

19. Keen, D. A. & Goodwin, A. L. The crystallography of correlated disorder. *Nature* **521**, 303–309 (2015).

20. Simonov, A. et al. Hidden diversity of vacancy networks in Prussian blue analogues. *Nature* **578**, 256–260 (2020).

21. Welberry, T. R. & Weber, T. One hundred years of diffuse scattering. *Crystallogr. Rev.* **22**, 2–78 (2016).

22. Weber, T. & Simonov, A. The three-dimensional pair distribution function analysis of disordered single crystals: basic concepts. *Z. Krist.* **227**, 238–247 (2012).

23. Overy, A. R. et al. Design of crystal-like aperiodic solids with selective disorder–phonon coupling. *Nat. Commun.* **7**, 10445 (2016).

24. Bennett, T. D. et al. Structure and properties of an amorphous metal-organic framework. *Phys. Rev. Lett.* **104**, 115503 (2010).

25. Ormrod Morley, D., Goodwin, A. L. & Wilson, M. Ring structure of selected two-dimensional procrystalline lattices. *Phys. Rev. E* **102**, 062308 (2020).

26. Li, X. & Sakai, T. Mass transport in polymer gels. In Sakai, T. (ed.) *Physics of Polymer Gels*, 137–150 (WILEY-VCH Verlag GmbH & Co. KgaA, 2020).

27. Dullien, F. A. L. *Porous media: Fluid transport and pore structure* (Academic Press, London, 1992), 2nd edn.

28. Yang, S. et al. A partially interpenetrated metal–organic framework for selective hysteretic sorption of carbon dioxide. *Nat. Mater.* **11**, 710–716 (2012).

29. Blunt, M. O. et al. Random tiling and topological defects in a two-dimensional molecular network. *Science* **322**, 1077–1081 (2008).

30. Eddaoudi, M. et al. Systematic design of pore size and functionality in isoreticular MOFs and their application in methane storage. *Science* **295**, 469–472 (2002).

31. Eddaoudi, M. et al. Porous metal–organic polyhedra: 25 Å cuboctahedron constructed from 12 $Cu_2(CO_2)_4$ paddle-wheel building blocks. *J. Am. Chem. Soc.* **123**, 4368–4369 (2001).

32. Zeng, X. et al. Complex multicolor tilings and critical phenomena in tetraphilic liquid crystals. *Science* **331**, 1302–1306 (2011).

33. Moshe, M., Bowick, M. J. & Marchetti, M. C. Geometric frustration and solid-solid transitions in model 2D tissue. *Phys. Rev. Lett.* **120**, 268105 (2018).

34. Venkatasubramanian, R., Siivola, E., Colpitts, T. & O'Quinn, B. Thin-film thermoelectric devices with high room-temperature figures of merit. *Nature* **413**, 597–602 (2001).

35. Gibson, Q. D. et al. Low thermal conductivity in a modular inorganic material with bonding anisotropy and mismatch. *Science* **373**, 1017–1022 (2021).

36. Coelho, A. A. *TOPAS* and *TOPAS-Academic*: an optimization program integrating computer algebra and crystallographic objects written in C++. *J. Appl. Cryst*. **51**, 210–218 (2018).

37. Willcott, M. R. MestRe Nova. *J. Am. Chem. Soc.* **131**, 13180 (2009).

38. Hafizovic, J. et al. The inconsistency in adsorption properties and powder XRD data of MOF-5 is rationalized by framework interpenetration and the presence of organic and inorganic species in the nanocavities. *J. Am. Chem. Soc.* **129**, 3612–3620 (2007).

39. Bruker. APEX4. Tech. Rep., Bruker AXS Inc., Madison, Wisconsin, USA (2022).

40. Sheldrick, G. M. SHELXT – integrated space-group and crystal-structure determination. *Acta Cryst. A***71**, 3–8 (2015).

41. Sheldrick, G. M. Crystal structure refinement with SHELXL. *Acta Cryst. C***71**, 3–8 (2015).

42. Dolomanov, O. V., Bourhis, L. J., Gildea, R. J., Howard, J. A. K. & Puschmann, H. Olex2: A complete structure solution, refinement and analysis program. *J. Appl. Cryst.* **42**, 339–341 (2009).

43. CrysAlis PRO. Agilent Technologies Ltd, Yarnton, Oxfordshire, England (2014).

44. Simonov, A. Meerkat. Version 0.3.7 (2020).

45. Weng, J. et al. K-space algorithmic reconstruction (KAREN): a robust statistical methodology to separate Bragg and diffuse scattering. *J. Appl. Cryst.* **53**, 159–169 (2020).

46. d'Acapito, F. et al. The LISA beamline at ESRF. *J. Sync. Rad.* **26**, 551–558 (2019).

47. Klementiev, K. V. XAFSmass. Freeware: www.cells.es/Beamlines/CLAESS/software/xafsmass.html (2012).

48. Lee, P., Citrin, P., Eisenberger, P. & Kincaid, B. Extended x-ray absorption fine structure—its strengths and limitations as a structural tool. *Rev. Mod. Phys.* **53**, 769–806 (1981).

49. Ravel, B. & Newville, M. ATHENA, ARTEMIS, HEPHAESTUS: data analysis for X-ray absorption spectroscopy using IFEFFIT. *J. Sync. Rad.* **12**, 537–541 (2005).

50. Rappe, A. K., Casewit, C. J., Colwell, K. S., Goddard III, W. A. & Skiff, W. M. UFF, a full periodic table force field for molecular mechanics and molecular dynamics simulations. *J. Am. Chem. Soc.* **114**, 10024–10035 (1992).

51. Manz, T. A. & Limas, N. G. Introducing DDEC6 atomic population analysis: part 1. Charge partitioning theory and methodology. *RSC Adv.* **6**, 47771–47801 (2016).

52. Martin, M. G. & Siepmann, J. I. Transferable potentials for phase equilibria. 1. United atom description of *n*-alkanes. *J. Phys. Chem. B* **102**, 2569–2577 (1998).

53. Potoff, J. J. & Siepmann, J. I. Vapor–liquid equilibria of mixtures containing alkanes, carbon dioxide, and nitrogen. *AIChE J.* **47**, 1676–1682 (2001).

54. Dubbeldam, D., Calero, S., Ellis, D. E. & Snurr, R. Q. RASPA: molecular simulation software for adsorption and diffusion in flexible nanoporous materials. *Mol. Simul.* **42**, 81–101 (2016).

55. Kühne, T. D. et al. CP2K: An electronic structure and molecular dynamics software package – quickstep: Efficient and accurate electronic structure calculations. *J. Chem. Phys.* **152**, 194103 (2020).

56. Perdew, J. P., Burke, K. & Ernzerhof, M. Generalized gradient approximation made simple. *Phys. Rev. Lett.* **77**, 3865–3868 (1996).

57. Grimme, S., Antony, J., Ehrlich, S. & Krieg, H. A consistent and accurate ab initio parameterization of density functional dispersion correction (DFT-D) for the 94 elements H–Pu. *J. Chem. Phys.* **132**, 154104 (2010).

58. Neder, R. B. & Proffen, T. Diffuse Scattering and Defect Structure Simulations: A cook book using the program DISCUS (Oxford University Press, Oxford, 2008).

59. Virtanen, P. et al. SciPy 1.0: Fundamental algorithms for scientific computing in python. *Nat. Meth.* **17**, 261–272 (2020).

60. Paddison, J. A. M. Ultrafast calculation of diffuse scattering from atomistic models. *Acta Cryst. A***75**, 14–24 (2019).

61. Stokes, H. T. & Hatch, D. M. Program for Identifying the Space Group Symmetry of a Crystal. *J. Appl. Cryst.* **38**, 237–238 (2005).

62. Panella, B., Hirscher, M., Pütter, H. & Müller, U. Hydrogen adsorption in metal–organic 36 frameworks: Cu-MOFs and Zn-MOFs compared. *Adv. Funct. Mater.* **16**, 520–524 (2006).

63. Perez, E. V., Balkus Jr, K. J., Ferraris, J. P. & Musselman, I. H. Mixed-matrix membranes containing MOF-5 for gas separations. *J. Membr. Sci.* **328**, 165–173 (2009).

Acknowledgements

The authors acknowledge the facilities and the scientific and technical assistance of Sydney Analytical, a core research facility at The University of Sydney.

Funding: The authors gratefully acknowledge financial support from the Australian Research Council (to C.J.K.; Grants DP150104620, DP190103130) and from the European Research Council

(to A.L.G.; Advanced Grant 788144). The authors also acknowledge support in the form of access to the UK's ARCHER2 supercomputer through the Materials Chemistry Consortium, funded by the E.P.S.R.C. (EP/R029431).

Author contributions: E.G.M. and L.J.C. synthesised and characterised the materials. E.G.M., E.M.S. and A.M. measured the x-ray diffuse scattering data, which were interpreted by E.G.M., E.M.S., A.M. and A.L.G. The Truchet-tile model was developed by E.G.M., E.M.S. and A.L.G. Crystallographic measurements and analysis were carried out by E.G.M., L.J.C., A.D.D., H.J.W., S.G.D., C.J.K. and A.L.G. Gas adsorption measurements were performed and analysed by E.G.M., L.J.C., A.D.D. and C.J.K. G.O.L. performed the EXAFS measurements, which were interpreted by E.G.M., G.O.L. and A.L.G. DFT and GCMC calculations were carried out and interpreted by T.P. and B.S. C.J.K. and A.L.G. conceived and coordinated the project. A.L.G. wrote the manuscript with input from all authors. All authors participated in discussions regarding the science presented in the manuscript.

Competing interests: The authors declare that they have no competing interests.

Data and materials availability: All crystallographic data have been deposited with the CCDC, with reference numbers 2203467–2203473. All other data needed to evaluate the conclusions in the paper are present in the paper or the Supplementary Materials.

Figure 1: Representative Truchet tilings. (A) Barcodes and QR codes store information in tilings of strips or pixels that break color-inversion symmetry. The average tile color, gray, is invariant under color inversion, but individual strips or pixels (examples outlined in red) store information in the way in which color inversion symmetry is broken. The patterns formed are Truchet tilings in the sense that individual tiles are lower in symmetry than the configurational average. (B) Decorating square tiles with a single arc can be used to generate Truchet tilings with curved paths. The positions of the square tiles are translationally periodic, but the continuous pattern produced by the arc decorations is aperiodic. Projecting any such tiling onto the underlying unit cell (shown in red) gives an average structure with partial occupancies. For large systems, one expects equal occupancies of each of the four possible arc orientations. (C) More complex Truchet tilings can be generated using a combination of different decorated and undecorated tiles. In this particular example, based on the trihexagonal tiling of the plane, the connected path of line decorations forms a single percolating network that spans the entire system.

Figure 2: Crystal structure of TRUMOF-1. (A) Representation of the average structure of TRUMOF-1 with OZn_4-centered clusters shown as red cuboctahedra and trigonally-symmetric ligand sites shown as gray triangles. (B) Interpretation of the crystallographic model at the ligand site in terms of a configurational average over three 1,3-bdc orientations and 25% linker vacancies. C atoms shown in black, O atoms in red, and H atoms omitted for clarity. (C) Related interpretation of the inorganic cluster as an average over 24 octahedral cluster orientations. Colors are as in panel B, with Zn atoms shown in gray. (D) The Truchet tiles used in our mapping correspond to (left to right) the pseudo-octahedral inorganic cluster orientations, the 1,3-bdc linker orientations, and the positions of ligand vacancies. Connecting these tiles to fill three-dimensional space forms networks that—like

the patterns in Fig. 1—are aperiodic. Note that the trigonal bipyramids pack such that any four combine to form a cube of the same dimensions as the (red) cluster cube. (E) One possible 1 × 1 × 1 approximant of the TRUMOF-1 structure with atom coordinates and cell geometry optimized using DFT. Note that the cluster positions are as in A, but that not all linker sites are occupied. The relation between cluster and cubic Truchet tile is emphasized for one cluster; likewise the connectivity between two clusters in the foreground and the corresponding link in the related Truchet tiling (D) are highlighted in green. (F) Representation of the (ordered) structure of MOF-5 in terms of its underlying tiling, for comparison against that given for TRUMOF-1 in panel D.

Figure 3: Computational and experimental validation of the TRUMOF-1 structure. (A) The relative lattice energies of different 1 × 1 × 1 (blue circles) and 2 × 2 × 2 (red squares) approximants are within a few kJ mol^{-1} of one another. Also included are the energies for geometry-optimized 2 × 2 × 2 supercells of two representative 1 × 1 × 1 approximants (yellow squares). The more disordered configurations are those at higher energy, for which the molar volume is largest. (B) Comparison of experimental and calculated single-crystal x-ray diffuse scattering in the (left) (*hk*0) and (right) (*hhl*) planes. The Bragg reflection positions are masked by white circles. (C) Comparison between experimental and calculated $r_x r_y 0$ cuts of the 3D-ΔPDF. Positive correlations are shown in red and negative in blue. (D) Comparison between the experimentally-derived crystallographic model for scattering density at the ligand site at 100 K (left) and that obtained by projection of DFT-relaxed structures onto the same site (right). Ellipsoids are shown at 50% probability.

Figure 4: Disordered pore network structure. A representative planar fragment of a TRUMOF-1 structure model, viewed down the [111] crystal axis. Only those 1,3-bdc molecules that link clusters

within this plane are shown. Each cluster is connected to six neighboring clusters, some of which will be in planes above or below that shown here. The surface of the solvent-accessible pores is shown as a gray outline. Note that, despite the periodic arrangement of inorganic clusters, the pore network is disordered. There is a qualitative similarity to the network structure shown in Fig. 1C.

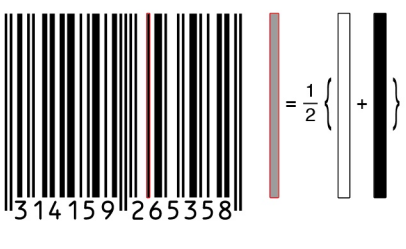

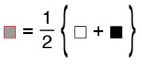

A

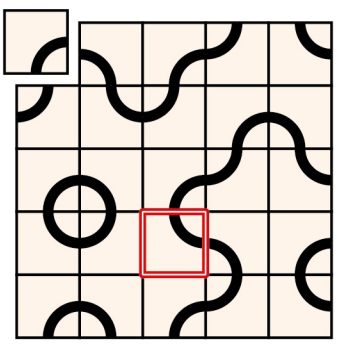

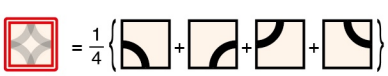

B

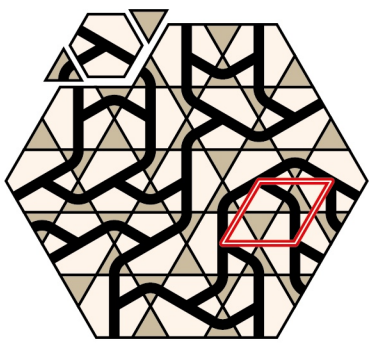

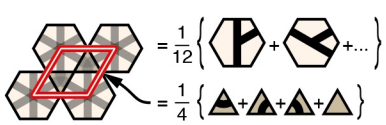

C

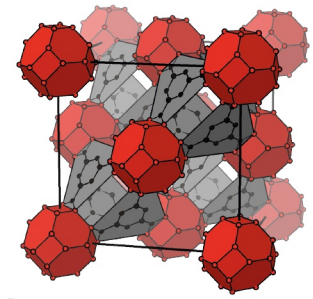

A

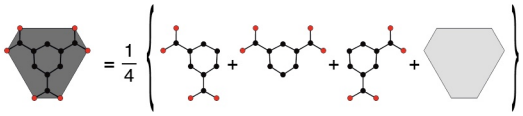

B

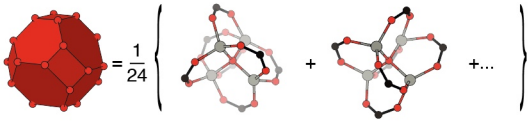

C

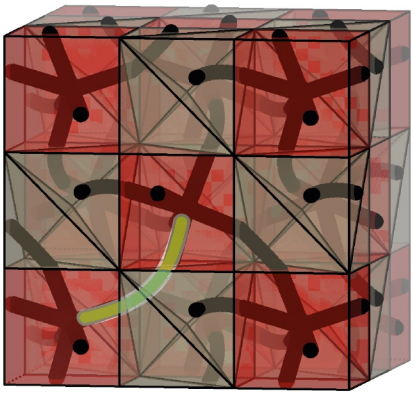

D

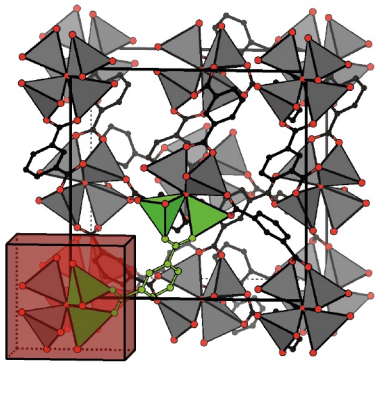

E

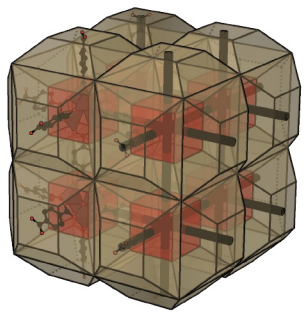

F

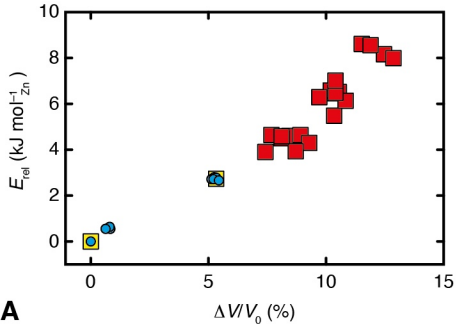
10
8
6
4
2
0
E_{rel} (kJ mol$^{-1}_{Zn}$)
0
5
10
15
$\Delta V/V_0$ (%)

A

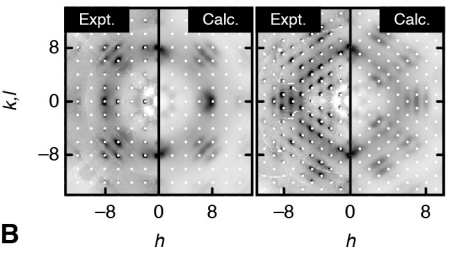
Expt.
Calc.
Expt.
Calc.
8
0
−8
k,l
−8
0
8
−8
0
8
h
h

B

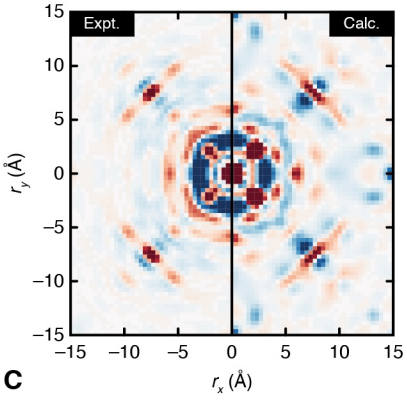
Expt.
Calc.
15
10
5
0
−5
−10
−15
r_y (Å)
−15
−10
−5
0
5
10
15
r_x (Å)

C

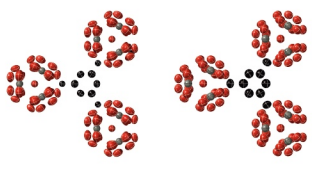

D

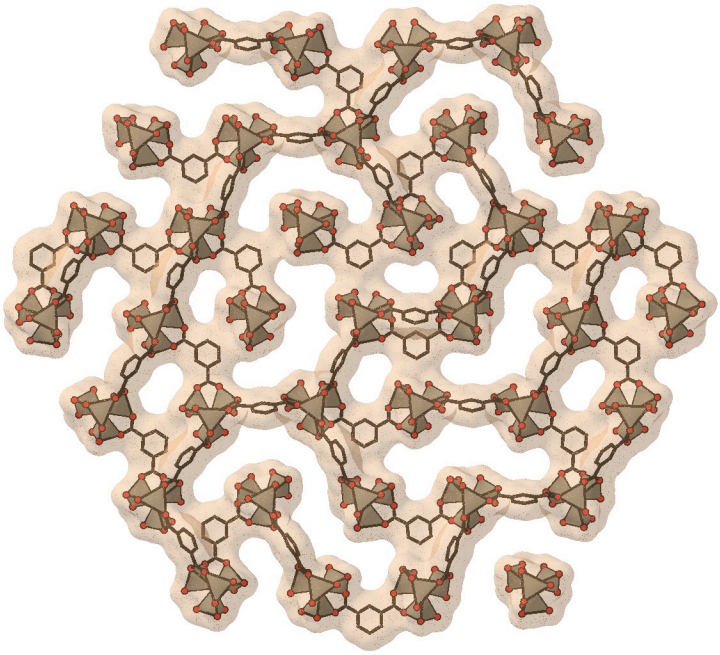

Science
AAAS

Supplementary Materials for

Truchet-tile structure of a topologically aperiodic metal–organic framework.

Emily G. Meekel, Ella M. Schmidt, Lisa J. Cameron, A. David Dharma, Hunter J. Windsor, Samuel G. Duyker, Arianna Minelli, Tom Pope, Giovanni Orazio Lepore, Ben Slater, Cameron J. Kepert, Andrew L. Goodwin

Correspondence to: cameron.kepert@usyd.edu.au or andrew.goodwin@chem.ox.ac.uk

This PDF file includes:

Other Supplementary Materials for this manuscript include the following:

Materials and Methods

Synthesis

TRUMOF-1 was synthesised by combining solutions of $Zn(NO_3)_2 \cdot 6H_2O$ (0.33 mmol) and 1,3-benzenedicarboxylic acid (0.33 mmol) in *N*,*N*-dimethylformamide (DMF; 5 mL). The resulting mixture was placed in a teflon-lined solvothermal vial and sealed. The vial was placed in an oven and heated to 110 ºC. After 14 h at this temperature, the system was slowly cooled to room temperature to afford TRUMOF-1 as colourless truncated pyramidal crystals. The crystals were isolated by filtration and washed three times with chloroform. Each washing cycle involved soaking TRUMOF-1 crystals in fresh $CHCl_3$ for 24 h, followed by filtration.

Molecular iodine could be incorporated into TRUMOF-1 by soaking single crystals, prepared as described above, in an iodine–cyclohexane solution (0.01 M) overnight. During this process, the crystals turned from colourless to purple. These purple crystals were washed with chloroform. Each washing cycle involved soaking TRUMOF-1:I_2 crystals in fresh $CHCl_3$ for 24 h, followed by filtration, and was repeated until the $CHCl_3$ filtrate was clear (approximately 4–6 repeats).

Single crystals of MOF-5 were synthesised following the method of (*6*). Solutions of $Zn(NO_3)_2 \cdot 6H_2O$ (0.1 mmol) and 1,4-benzenedicarboxylic acid (0.1 mmol) in dried *N*,*N*-diethylformamide (1 mL and 3 mL, respectively) were combined and the resulting mixture placed in a teflon-lined solvothermal vial. The vial was heated to 100 ºC for a period of 48 h. On cooling back to room temperature, the vial contained colourless cubic crystals of MOF-5. The crystals were washed three times with dichloromethane. Each washing cycle involved soaking MOF-5 crystals in fresh CH_2Cl_2 for 24 h, followed by filtration.

Powder X-ray Diffraction

Laboratory powder X-ray diffraction patterns of TRUMOF-1 and MOF-5 were collected at ambient temperature using a high-intensity Bruker D8 Advance Eco diffractometer equipped with a Cu Kα source (λ = 1.54 Å) and a fluorescence-filtering LYNXEYE XE-T detector. Samples were prepared by grinding single-crystal samples and allowing the powders produced to dry in air. Thin layers of the powder samples were deposited on the sample holder using a minimum amount of vacuum grease. The resulting diffractograms are shown in Fig. S1.

In order to verify the phase purity of these samples, we carried out Pawley refinements using the TOPAS software (*36*). For TRUMOF-1, we obtained an excellent fit-to-data using a refinement model containing a single phase with $F\bar{4}3m$ space-group symmetry; the refined lattice parameter so obtained was a = 15.5094(3) Å (at room temperature). Likewise, we were able to fit the MOF-5 diffraction pattern using a single-phase model with $Fm\bar{3}m$ space-group symmetry; the resulting lattice parameter was a = 25.8317(11) Å. Both fits are shown in Fig. S1.

Nuclear Magnetic Resonance

In order to confirm the chemical composition of bridging ligands present within TRUMOF-1, we used a combination of ^{1}H and ^{13}C NMR measurements. All NMR measurements were performed on a 2-channel Bruker AVIII 400 nanobay instrument (VIII HD 400) running TOPSPIN 3 equipped with a 5-mm z-gradient broadband multinuclear probe with variable temperature accessories and a 24-position SampleCase robotic sample changer. Data analysis was performed using the software MestreNova (*37*).

We used an acid-digestion approach to dissolve TRUMOF-1 samples. A DCl/D_2O solution (33%) was prepared and a minimum of this acid solution was used to dissolve TRUMOF-1

crystals. The resulting solution was added to deuterated dimethylsulfoxide (DMSO) for NMR analysis. For comparison studies, we also dissolved samples (5–10 mg) of 1,3-benzenedicarboxylic acid (1,3-bdc) and 1,3,5-benzenetricarboxylic acid (1,3,5-btc) in a small quantity of deuterated DMSO.

The resulting ^{1}H and ^{13}C NMR spectra are shown in Fig. S2. We find that digested TRUMOF-1 samples contain intact 1,3-bdc linkers. An additional peak in the ^{1}H NMR spectrum indicates that our solvent-exchange protocol results in a small quantity of remnant DMF retained within TRUMOF-1 crystals. There is no evidence to support incorporation of 1,3,5-btc linkers within TRUMOF-1, as the corresponding peaks are not present in the spectra of TRUMOF-1 samples. This point will become important in the context of interpreting the single-crystal X-ray diffraction patterns of TRUMOF-1.

Infrared and Raman Spectroscopy

We used a combination of IR and Raman spectroscopy to characterise the vibrational spectrum of TRUMOF-1 and to determine the degree of similarity or difference to that of MOF-5. The FT-IR absorbance spectra of MOF-5 and TRUMOF-1 were recorded by placing dried samples onto a Shimadzu IRAffinity-1. A background scan was taken before each measurement in order to ensure the previous sample had been completely removed. Data were processed using the LabSolutions IR software. Raman scattering spectra were acquired using a Renishaw InVia Qontor confocal spectrometer. Samples were excited using a Renishaw plc RL785 red diode laser outputting an excitation wavelength of 785 nm (25% laser power, 40–50 mW) and were referenced internally with respect to silicon at 520.5 ± 0.1 cm^{-1}. Single crystalline samples of TRUMOF-1 and MOF-5 were loaded onto an aluminium plate and then a Leica long 50× objective was used to focus the laser beam perpendicularly onto the sample. Spectra were recorded on a Renishaw Centrus 2957N7 CCD detector using 10 s exposure times averaged over 3 accumulations. Data were processed using Renishaw's WiRE software, with baseline subtractions and cosmic ray removal as required.

The measured IR and Raman absorption spectra are shown in Fig. S3. We observe qualitatively similar distributions of spectral weight for the two samples, which suggests that the bonding arrangements are similar in the two compounds.

Thermogravimetric Analysis

Thermogravimetric analysis (TGA) of both TRUMOF-1 and MOF-5 samples was performed to compare their relative stability. Measurements were carried out using a Mettler Toledo TGA/DSC 1 system operated under flowing N_2 with a ramp rate of 5 ºC min^{-1} from 25 to 700 ºC. Prior to the experiment, TRUMOF-1 and MOF-5 samples were soaked in DCM for two consecutive days. The samples were left to dry at room temperature under vacuum. Our results are shown in Fig. S4, where relative mass values have been normalised to the absolute value measured at 700 ºC.

Both TGA traces reflect four distinct temperature regimes, as discussed in (*38*). For temperatures up to about 100 ºC, there is a small degree of mass loss associated with surface solvent. Over the temperature range 100–300 ºC, we observe gradual loss of adsorbed solvent to give the evacuated MOF. This regime is followed by a plateau that extends up until about 400 ºC. Thereafter the organic component of the frameworks decompose. We observe similar decomposition temperatures for MOF-5 and TRUMOF-1.

Single-Crystal X-ray Diffraction: Average Structure Determination and Refinement

The single crystal diffraction pattern of TRUMOF-1 was measured using a Bruker FR591-D85-ApexII diffractometer equipped with an Incoatec IμS 2.5 rotating anode source, D85 four-circle kappa goniometer, and Incoatec Quazar multilayer optics. The instrument outputted mirror-monochromated Mo-Kα (λ = 0.71073 Å) radiation and was fitted with a Bruker Apex-II CCD area detector which was equipped with an Oxford Cryosystems Cryostream 700 for temperature control. A washed crystal of TRUMOF-1 was isolated directly with $CHCl_3$, evacuated, and then mounted onto a 0.2 mm diameter MiTeGen loop using Paratone-N oil as a cryoprotectant. The crystal was then attached to the instrument goniometer and cooled to the desired initial temperature (100 K) before data were collected about ϕ and ω rotations. Unit cell determination, data integration, frame scaling, and absorption corrections (multi-scan implemented in SADABS with beam profile correction) were performed in APEX4 (*39*).

A structure solution in the non-centrosymmetric cubic space group $F\bar{4}3m$ was obtained by intrinsic phasing methods from SHELXT (*40*) and was refined by a full-matrix least-squares on all unique F^2 values using SHELXL (*41*) as implemented within OLEX2-1.5 (*42*). An initial solution showed clearly the presence of OZn_4 tetrahedra centred on the 4*a* Wyckoff position. The remaining electron density extended between neighbouring tetrahedra, forming molecular arrangements that resembled the trigonally symmetric molecule 1,3,5-btc. The centre of this molecular scattering was the 16*e* site, which has 3*m* point symmetry. Because our NMR measurements showed conclusively the presence of 1,3-bdc and absence of 1,3,5-btc molecules in TRUMOF-1, we proceeded to test whether this ligand-site scattering density was consistent with partial occupancy by different orientations of 1,3-bdc units. In such a model, the occupancies of the carboxylate C and O atoms should be linked (we label these C1 and O2, respectively); likewise the occupancies of the benzene C atoms should all be identical (these atoms appear as two crystallographically-distinct sites, which we label C2 and C3). A simplified refinement model in which site occupancies were allowed to vary, subject to these constraints gave the occupancies listed in Table S1. In order to avoid strong covariance between site occupancies and atomic displacement parameters, we used a single common U_{iso} value for all linker atoms. The key result is that the occupancies of C1 and O2 refine to values close to 0.5, and those of C2 and C3 close to 0.75; these are the values expected for the anticipated crystal stoichiometry $[OZn_4][1,3\text{-bdc}]_3$.

Having established that the linker site reflects a configurational average over three orientations of 1,3-bdc units, we developed a full structural model for refinement against our single-crystal diffraction data. The asymmetric unit of this model is shown in Fig. S5. In this model, C2 is split into two atoms C2A/C2B with identical coordinates and displacement parameters. These split sites reflect the (1,3)- and 5-positions of the 1,3-bdc molecule. The H atom bound at the 5-site is given the label H2B. The C3 site corresponds to the (2,4)-positions of the 1,3-bdc molecule, and is connected to the corresponding H3 atom.

All non-hydrogen atoms could be treated by an unrestrained anisotropic refinement unless otherwise stated. The position of H2B could not be located from the Fourier difference map and so had to be added in its calculated position and refined using riding thermal parameters. The second hydrogen site H3 could not be located from the Fourier difference map either, but also could not be added in its calculated position due to the symmetry imposed by the selected space group. Thus, the H3 site had to be added manually and refined with considerably strong geometric restraints to achieve a physically realistic C–H distance. DFIX was employed for this purpose, and a value of 0.95 was chosen to achieve a similar bond length as for the constrained

H2B site. The thermal parameter U_{iso} for H3 was also fixed to be the same as H2B. The 1,3-distance between H3 and its ortho carbon sites C2A and C2B was unrestrained, but to achieve an overall flat geometry of the 1,3-bdc linker, a FLAT command was applied to C2A, C2B, and all of the other symmetry generated positions that make up the central C_6 ring. The 1,3-bdc linker is equally disordered over three different orientations by the imposed symmetry of the $F\bar{4}3m$ space group. Additionally, because of the chemistry of the TRUMOF-1 system, each carbon site in the C_6 ring is only 75% occupied. However, for C2A and C2B (which share a common position), their occupancies were fixed at 50% and 25%, respectively, to achieve a 75% overall occupancy and to reflect the extent of there being a 25% vacancy of the 1,3-bdc unit. Accordingly, C2A and C2B had their atomic coordinates and thermal parameters fixed using the EXYZ and EADP constraints. Finally, we included a refineable inversion twin fraction.

Crystal data and refinement statistics for the 100 K data set, which is representative of all temperature points, are given in Table S2. We used an entirely equivalent approach to obtain structural models for six further temperature points: namely, 140, 180, 220, 260, 300, and 340 K. The corresponding .cifs and checkcifs are provided as Data File S5; all structures have been deposited with the CCDC and have reference numbers 2203467–2203473. Selected variable-temperature structural parameters are listed in Data Files S1 and S2. The X-ray powder diffraction pattern calculated from our 300 K model is compared against experiment in Fig. S6.

Single-Crystal X-ray Diffuse Scattering

All single-crystal X-ray diffuse scattering measurements of (guest-containing) TRUMOF-1 crystals were collected on a Rigaku Synergy S diffractometer fitted with a Dectris EIGER2 R 1M detector. All data sets were collected under copper radiation (λ = 1.5406 Å). Crystals were mounted on a 0.2 mm diameter MiTeGen loop using Paratone-N oil as a cryoprotectant. An exposure time of 200 s was needed to detect diffuse features at room temperature (300 K). Each measurement involved a full ϕ-scan carried out in a single run.

CrysAlisPro was used for indexing, determination and refinement of the orientation matrix (*43*). For the diffuse scattering analysis the scattering data were reconstructed on a three-dimensional grid defined by $-20 \le h,k,l \le +20$ with voxel sizes of $\Delta h = \Delta k = \Delta l = 0.1$ r.l.u., resulting in an array of 401 × 401 × 401 voxels. For this purpose, the crystal orientation as refined with CrysAlisPro was converted using a customized code to serve as input for the Meerkat program (*44*). After careful inspection of the diffraction data it was observed that the diffuse scattering also follows $m\bar{3}m$ Laue symmetry. The data were subsequently averaged for $m\bar{3}m$ Laue symmetry using Meerkat (*44*).

Further data treatment for the experimental 3D-ΔPDF generation consisted of Bragg peak and background subtraction. Bragg peak removal was performed using the KAREN algorithm (*45*), which is based on an outlier rejection: in the three-dimensional reconstruction Bragg peaks only extend over a few voxels on well-defined positions. The intensity of these voxels is much larger than the intensity of the diffuse scattering and therefore recognised as outliers. The background caused by scattering from air and/or Paratone-N oil was estimated as a smooth, radially symmetric background function which was subtracted from the data. To reduce the effect of Fourier ripples in the generation of the 3D-ΔPDF, the background-subtracted data were multiplied with a Gaussian fall-off that smooths the edges of the measured reciprocal space section (see (*45*)). The FFT algorithm as implemented in Meerkat (*44*) was used to obtain 3D-ΔPDFs shown in Fig. 3 of the main text.

An example of the scattering patterns recorded using conventional exposure times is given in Fig. S7. By contrast, Fig. S8 shows reconstructed *hk*0 and *hhl* layers of a TRUMOF-1 crystal with $CHCl_3$ solvent guests incorporated, collected at an exposure time of 200 s. Soaking the crystals in an iodine-cyclohexane solution and collecting data at 200 s per frame (at 300 K) resulted in the diffuse features running on and through the Bragg peaks to gain in relative intensity (Fig. S9). Performing an identical data collection on the same iodine-soaked crystal at a temperature of 120 K led to a decrease in intensity of the diffuse scattering on the Bragg peaks (Fig. S10). Yet the diffuse streaks running through the Bragg peaks on the diagonals keep their intensity, indicating the disorder to be static. Note that the diffuse ring around the origin was caused by ice formation on the crystal. The effect of background subtraction is visible by comparing the non-background subtracted intensities in Figs. S8–S10 with the diffuse scattering shown in Fig. 3 of the main text.

Extended X-ray Absorption Fine Structure

X-ray absorption spectroscopy (XAS) measurements were performed at the LISA beamline (BM-08 (*46*)) at the European Synchrotron Radiation Facility (ESRF, Grenoble, France) using the Zn K-edge (9658.6 eV). Samples were measured using a pair of Si(311) flat monochromator crystals, providing an energy resolution of $\sim 4 \times 10^{-5}$ ($\Delta E/E$). Si-coated focusing mirrors ($E_{\text{cut-off}} \sim 16$ keV) were used for harmonic rejection. In order to prevent beam-damage on samples, data were collected with a wide beam (approximately 2×2 mm^2) and low flux (approximately 2×10^9 ph s^{-1}). Measurements were performed in transmission mode at room temperature. The step size for the XANES region was 0.5 eV; the post-edge EXAFS region of the spectrum was acquired with a fixed *k*-step width of 0.025 Å^{-1}.

Both the TRUMOF-1 and MOF-5 samples for the EXAFS experiment were prepared as pellets using a manual hydraulic press. To prevent the crystal samples from collapsing, both samples were gently ground to a fine powder using a pestle and mortar. The required weight of each sample was calculated using the Viper XAFS mass software/widget (*47*), taking into account the energy required at the Zn K edge (9659 ± 50 eV) and the surface area of the pellets (1.237 cm^2). To the sample, approximately 100 mg of cellulose was added. The two components were then mixed and ground together using the pestle and mortar, before gently depositing onto a macro-micro KBr pellet die. After fitting, the die was placed on the hydraulic press, which was used to increase the pressure to no higher than 2 bar, creating the pellet. Note that the pressure was intentionally kept at a low value to prevent the porous samples from collapsing. The pellets were removed from the die and pressed between kapton (polyimide) tape, which in turn was fitted onto the sample holder to be kept in the beam.

Standard procedures (*48*) were followed to extract the structural EXAFS signal ($\kappa \cdot \chi(\kappa)$): pre-edge background removal, spline modelling of bare atomic background, edge step normalization using a far above the edge region, and energy calibration using the software ATHENA (*49*). The resulting EXAFS signals and their Fourier transforms are shown in Fig. S11. Pearson correlation coefficients calculated for these data show very high similarities (0.99). So the key observation is that the EXAFS data measured for MOF-5 and TRUMOF-1 are essentially indistinguishable, indicating that Zn atoms are in the same local environments in the two materials.

Gas Adsorption

To prepare a TRUMOF-1 sample for adsorption measurements, $CHCl_3$-exchanged TRUMOF-1 crystals were left to dry in air before weighing in a pre-dried and weighed BET tube. The TRUMOF-1 crystals were activated at 150 ºC under dynamic vacuum at 10^{-4} mbar for 120 h to remove any solvent. The degassed sample mass was measured prior to analysis and determined to be 45.9 mg. Nitrogen, hydrogen, methane and carbon dioxide adsorption isotherms were recorded at low pressure (0–1.2 bar) by a volumetric method using a Micromeritics 3Flex instrument. The isotherms are shown in Fig. S12. Gas adsorption measurements were performed using ultra-high purity gas from BOC gas Australia (Grade 5.0). Isosteric heats of adsorptions were calculated from measurements taken at two different temperatures; 77 K and 87 K for hydrogen and 273 K and 293 K for methane and carbon dioxide (see Figs. S12 and S13, and Table S3). The BET surface area was calculated using the nitrogen gas adsorption data collected at 77 K, resulting in a value of 765 $m^2\ g^{-1}$. Analysis of the data including the calculation of the BET surface area and heat of adsorption was performed using the MicroActive for 3FLEX software.

Grand Canonical Monte Carlo Simulations

We performed Grand Canonical Monte Carlo (GCMC) Simulations to determine single-component adsorption isotherms of CH_4 and CO_2, at 273 and 293 K. The pressure range of the isotherms was chosen to be 0–1 bar with a step-size of 0.01 bar. The Lennard-Jones (LJ) parameters for the framework were assigned from the Universal Force Field (UFF) (*50*) and the Density Derived Electrostatic and Chemical (DDEC6) method (*51*) was used for charge parameterisation. The electrostatic interactions in the CO_2 simulations were calculated using the Ewald summation method. The Transferable Potentials for Phase Equilibria (TraPPE) force field was deployed for both adsorbates. CH_4 was modelled as a single united atom site (*52*), whilst CO_2 comprised three LJ sites (*53*). LJ interactions were truncated at 13.0 Å with tail corrections applied and each cell was expanded to abide by the minimum image convention. Lorentz–Berthelot mixing rules were used to compute the adsorbate-MOF interactions. A total of 5×10^4 cycles were used for system initialisation and a further 5×10^4 cycles were carried out to average the thermodynamic properties. Translation, rotation, reinsertion, insertion, and deletion Monte Carlo moves were attempted in the simulation cell. All Monte Carlo simulations were carried out using the RASPA software (*54*). The calculated adsorption isotherms are shown in Fig. S14. We consider the comparison with experiment (Fig. S12) to be remarkably good, considering the following limitations of both experiment and computational approaches used: (i) it is difficult to guarantee that activation/desorption of solvent is complete; (ii) there may be some non-volatile pore contents; and (iii) our GCMC implementation neglects any contribution from framework flexibility, since the framework is treated as rigid.

Approximant Generation

Each cluster site in the $F\bar{4}3m$ average-structure solution is surrounded by 12 carboxylate ions with 50% occupancy. Our initial task in generating TRUMOF-1 approximants is to assign binary occupancies to each carboxylate site subject to two constraints: (i) each OZn_4 unit must coordinate exactly six carboxylates, disposed approximately octahedrally, and (ii) the carboxylate occupancies of neighbouring OZn_4 clusters must be realisable in terms of the presence or absence of 1,3-bdc units on the ligand site. We used a custom Monte Carlo (MC) code and a simulated annealing approach to generate approximants satisfying these two constraints. The algorithm implemented was developed as follows.

We begin by noting that there are in principle $C(12,6) = 924$ ways of occupying exactly six of the 12 carboxylate sites around each cluster. Many of these possibilities involve unphysically close O–O contacts and need not be considered. For example, the 12 sites divide into 6 pairs disposed along the ⟨100⟩ directions (Fig. S15(a)). The O–O distances within pairs are so small that only one of each pair might be occupied at any one time, reducing the number of possibilities to $2^6 = 64$. Even amongst these 64 local configurations there are cases with unfeasible geometries and energies many hundreds of kJ mol^{-1} above the ground state (Fig. S15(b)). The decoration that maximises O–O contact distances is approximately, but not exactly, octahedral (Fig. S15(c)); note that there is no decoration that has octahedral symmetry. This maximally-distributed configuration has trivial point symmetry and so there are 24 equivalent carboxylate decorations with this same local geometry (this being the ratio of the orders of the crystallographic $\bar{4}3m$ point symmetry at the cluster site and the cluster point symmetry). These 24 symmetry-equivalent configurations correspond to the 24 different orientations of the corresponding Truchet tile (red cube) shown in Fig. 2D of the main text.

Our MC algorithm assigns cluster geometry orientations as a 24-state Potts variable; these are the fundamental degree of freedom. Initially, each cluster site in an appropriately-chosen supercell (e.g. $2 \times 2 \times 2$) was assigned randomly one of the 24 equivalent states and the corresponding carboxylate sites occupied accordingly. The initial MC energy was determined by cycling through the 1,3-bdc linker sites and counting the number of occupied carboxylate ligands converging on that site. If this number were 0 or 2 then the corresponding energy term was zero: the former case allows for a bdc vacancy, and the latter can always be accommodated by a 1,3-bdc linker in a suitable orientation. By contrast, if either just 1 or all 3 carboxylate sites were occupied, then the energy was incremented by 1—there being no way of arranging 1,3-bdc linkers to give this carboxylate occupancy. Defined in this way, the total MC energy is zero if and only if the cluster decorations are consistent with 75% occupancy of the linker sites by 1,3-bdc molecules. We drove the system towards this ground state by repeatedly choosing different cluster orientations as the MC move, and by using simulated annealing to gradually tighten the MC acceptance criterion until the system energy converged to zero.

The final stage in our approximant generation was to allow the configuration to relax into a state with idealised $[OZn_4][OOCR]_6$ node geometries. Starting from one of our MC configurations, we treated the 1,3-bdc molecules and $[OZn_4]$ clusters as rigid bodies with translational and rotational degrees of freedom. We could now define a new MC energy based on the squared distance between carboxylate oxygen positions and the 'ideal' positions for the corresponding OZn_4 cluster. We again used a simulated annealing approach to relax the configuration, proposing and rejecting small rigid-body translations and rotations of both bdc and OZn_4 units in each MC loop. An additional closest-approach constraint was used to ensure that no atom positions overlapped. Note that the framework connectivity remained hardwired from the initial MC process. These relaxed configurations were used as input for DFT geometry optimisation.

Geometry Optimisation

Full cell optimisations were carried out using the Quickstep module of the CP2K package (*55*). We used the DZVP MOLOPT basis sets for all atoms, the PBE functional (*56*) and the "D3" van der Waals correction scheme (*57*). A 800 Ry cut-off was used in conjunction with a reference cell for smooth optimisation of the cell parameters and atomic coordinates until the forces on the atoms were less than 0.6 kJ mol^{-1} Å^{-1}. No atomic constraints were applied during

the relaxation and no symmetry was imposed upon the cell parameters or coordinates (in effect the cells are relaxed in *P*1). Summaries of the optimised cell parameters and relative energies are given in Data Files S3 and S4 for the ten 1 × 1 × 1 and twenty 2 × 2 × 2 approximants, respectively. Data File S4 also includes results for two 2 × 2 × 2 supercells of 1 × 1 × 1 approximants (labelled '1_2' and '2_2'). The corresponding atomic coordinates for all files are included in a series of .cif files provided as Data File S6. The geometry-optimised structure of one representative 2 × 2 × 2 approximant is illustrated in Fig. S16.

Diffuse Scattering and 3D-ΔPDF Calculation

The 20 independent DFT-relaxed 2 × 2 × 2 supercell configurations were imported into the DISCUS program (*58*) for calculating the diffuse scattering and the corresponding 3D-ΔPDFs. The X-ray scattering was calculated on the Bragg positions of the supercells, with the same reciprocal space coverage as the experiment (i.e. $-40 \le h,k,l \le +40$). The overall $F\bar{4}3m$ symmetry of the average structure is not maintained locally in the DFT-relaxed cells, which only cover 2 × 2 × 2 unit-cells of the parent structure. To mimic the distribution of configurations in a crystal—as we expect in our measurement—the calculated diffraction patterns of 20 configurations were averaged and the result was averaged for $m\bar{3}m$ Laue symmetry. To obtain the 3D-ΔPDFs the Bragg Peaks of the parent structure that fulfilled the *F*-centering reflection conditions were eliminated. The missing intensity was interpolated from the surrounding voxels using a custom script using the SciPy interpolate package (*59*). The same Gaussian falloff as for the experimental data was applied to reduce the effect of Fourier ripples in the calculated 3D-ΔPDF which is shown in the main text.

Note that the maximum *h*,*k*,*l* used in the calculation of the diffuse scattering determines the voxel size in the PDF: Here we used $-20 \le h,k,l \le +20$ for the parent structure reciprocal space grid, hence the PDF-voxels have a size of $\Delta u = \Delta v = \Delta w = 0.025$ r.l.u. The voxel size in reciprocal space determines the maximum value of *u*,*v*,*w* in the PDF map: for the experimental data we have $\Delta h = \Delta k = \Delta l = 0.1$, which gives $-5 \le u,v,w \le 5$ for the PDF. In the simulated data the size of the super-cell restricted the reciprocal space voxel size $\Delta h = \Delta k = \Delta l = 0.5$, which gives $-1 \le u,v,w \le 1$ for the PDF.

For the comparison of the measured and calculated diffuse scattering patterns shown in Fig. 3C of the main text, the calculated diffuse scattering was resampled to a finer reciprocal space grid. For this we use the Lanczos resampling approach as described in (*60*). An additional smoothly-varying circularly-symmetry transparent background image was included to mimic the remnant air-scatter background apparent in the experimental data. The diffuse scattering pattern and 3D-ΔPDF calculated from Truchet-tile models of TRUMOF-1 prior to subsequent DFT geometry optimisation show a much worse match to experiment (Fig. S17), serving to highlight the sensitivity of the two functions to the precise structural relaxations driven by the aperiodic framework connectivity.

Anisotropic Displacement Parameter Calculation

Because the optimised structures calculated using DFT involve relaxation of atoms away from their high-symmetry positions, we were able to extract from these configurations a measure of the expected static-disorder contribution to the atomic displacement parameters. For each of the 20 DFT-relaxed 2 × 2 × 2 supercell configurations, and using a custom script, the origin shift was determined by the collective average displacement of the O1 atoms. This origin shift was

subtracted from all atom coordinates and then $F\bar{4}3m$ crystal symmetry was applied. The average positions of all atoms in the asymmetric unit were determined, and the U_{ij} values calculated from the second moments of the distributions observed (Table S4). These values are compared against the experimental values extrapolated to 0 K in Fig. S18.

Supplementary Text

Approximant Enumeration

In order to determine the number of symmetry-distinct approximants for a given supercell size, we used the following approach. Two approximants are considered symmetry related if there exists a combined translation and point group operation that maps the connectivity of one onto the other. For the specific case of $1 \times 1 \times 1$ approximants, these combined symmetry elements are precisely the elements of the $F\bar{4}3m$ space group. Considering first this case, we note that there are four clusters in the approximant cell, each of which is in principle capable of adopting any one of 24 equivalent orientations. Hence there are $24^4 = 331{,}776$ possible cluster arrangements, not all of which will correspond to Truchet tilings—many will not be realisable once the constraint of 1,3-bdc linker connectivity is imposed. To reduce the search space, we fix the orientation of the cluster at the approximant cell origin. This is allowed because any viable approximant structure can be mapped onto an equivalent structure with this reference cell-origin-cluster orientation by applying one of the $\bar{4}3m$ point symmetry operations. The $24^3 = 13{,}824$ cluster orientation combinations that remain were then considered one-by-one and the MC energy (described above) determined in each case. Exactly four combinations gave zero (ground-state) MC energies, and two of these are related to one another by application of a $F\bar{4}3m$ symmetry operations. We used the FINDSYM tool (*61*) to characterise these three symmetry-distinct approximants. The first and second have $P\bar{4}$ and $P\bar{2}_1$ symmetry, respectively; the corresponding unit cells are oriented as for the original $F\bar{4}3m$ cell itself. The third symmetry-distinct $1 \times 1 \times 1$ approximant has *Pc* symmetry and a unit cell with axes $\mathbf{a}' = \frac{1}{2}\mathbf{a} + \frac{1}{2}\mathbf{b}$, $\mathbf{b}' = -\frac{1}{2}\mathbf{a} + \frac{1}{2}\mathbf{b}$, $\mathbf{c}' = -\frac{1}{2}\mathbf{a} - \frac{1}{2}\mathbf{b} + \mathbf{c}$. In Data File S3, configuration 1 is of the first type, configurations 2–6 are of the second type, and configurations 7–10 are of the third type. Despite our using different explicit realisations of the three symmetry-distinct configurations, the DFT-relaxed energies of these configurations respect the underlying symmetry: all ten energy values partition into three groups that correspond to the three symmetry-distinct connectivities. The minor numerical differences that persist reflect typical variations in DFT energies when symmetry constraints are removed (all our relaxations were performed in *P*1 symmetry).

While in principle a similar approach might be used to enumerate viable Truchet-tile $2 \times 2 \times 2$ approximants, there is a combinatorial problem involved in practically doing so. A $2 \times 2 \times 2$ approximant contains 32 clusters, so there are $24^{31} \sim 10^{43}$ combinations to be tested. This is beyond our computational capabilities. If the fraction of orientation combinations that admit viable Truchet-tile connectivities is similar to that in the $1 \times 1 \times 1$ case ($\sim 0.03\%$) then there are about 1.8×10^{39} symmetry-distinct combinations. We expect this to be a considerate overestimation of the true number, since the number of translational symmetry elements that map equivalent configurations onto another is also much larger than for the $1 \times 1 \times 1$ case. Nevertheless, we expect the space of $2 \times 2 \times 2$ symmetry-distinct approximants to be very much larger than that of the $1 \times 1 \times 1$ approximants. The 20 specific examples that we have considered in our own study were obtained using the Monte Carlo algorithm described above. Because the

cluster orientations were initialised randomly, and subsequent MC moves were generated randomly, we do not expect any strong bias in the selection of these representative approximants from amongst the much larger landscape of all possible $2 \times 2 \times 2$ symmetry-distinct approximants.

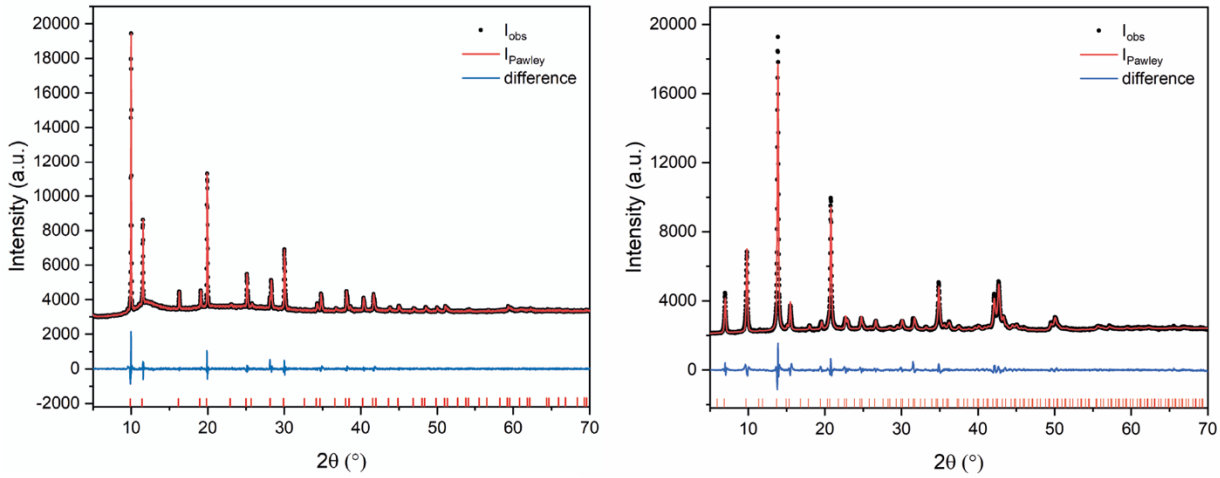

Fig. S1.

Powder X-ray diffraction measurements (λ = 1.54 Å) of TRUMOF-1 (left) and MOF-5 (right). Data are shown as black points, Pawley fits as red lines, and the difference (fit – data) shown as blue lines. Reflection positions are shown as vertical tick marks.

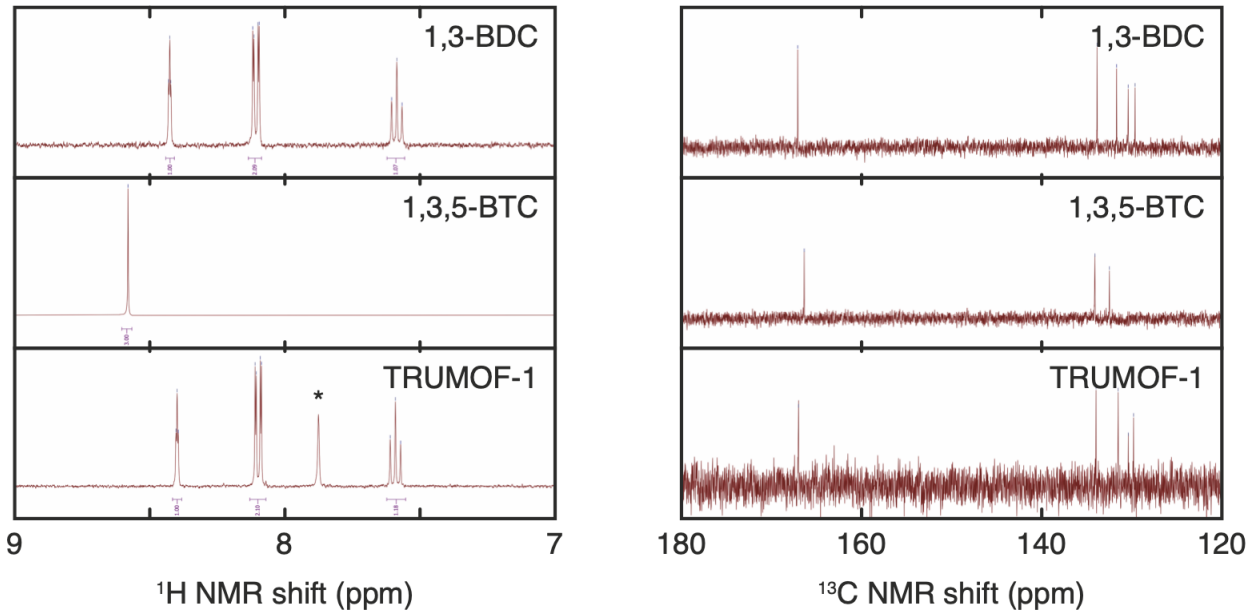

Fig. S2.

NMR characterisation of acid-digested TRUMOF-1 crystals and comparison to 1,3-bdc and 1,3,5-btc samples: (left) ^{1}H and (right) ^{13}C NMR spectra for the three samples as measured in deuterated DMSO. The regions shown cover the shifts associated all aromatic C and H atoms, together with those of the carboxylic acid C environments. The only signals not included in these regions arise from solvent. Detected signals are as follows. 1,3-bdc ^{1}H δ 8.43 (t, J = 1.7 Hz, 1H), 8.11 (dd, J = 7.7,1.8 Hz, 2H), 7.59 (t, J = 7.7 Hz, 1H); ^{13}C δ 167.08 (s), 133.86 (s), 131.70 (s), 130.41 (s), 129.65 (s). 1,3,5-btc ^{1}H δ 8.60 (s, 3H); ^{13}C δ 166.36 (s), 134.05 (s), 132.43 (s). Digested TRUMOF-1 ^{1}H δ 8.40 (t, J = 1.7 Hz, 1H), 8.09 (dd, J = 7.8,1.8 Hz, 2H), 7.58 (t, J = 7.8 Hz, 1H), and a solvent peak originating from DMF (indicated by an asterisk); ^{13}C δ 166.98 (s), 133.94 (s), 131.49 (s), 130.36 (s), 129.77 (s).

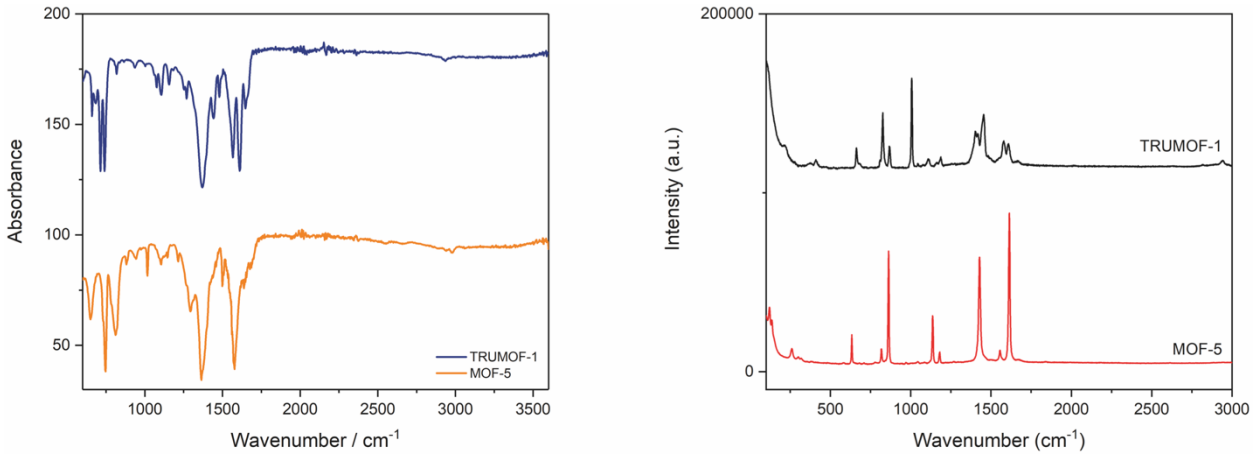

Fig. S3.

Vibrational spectra of TRUMOF-1 and MOF-5 measured using (left) FT-IR and (right) Raman spectroscopy.

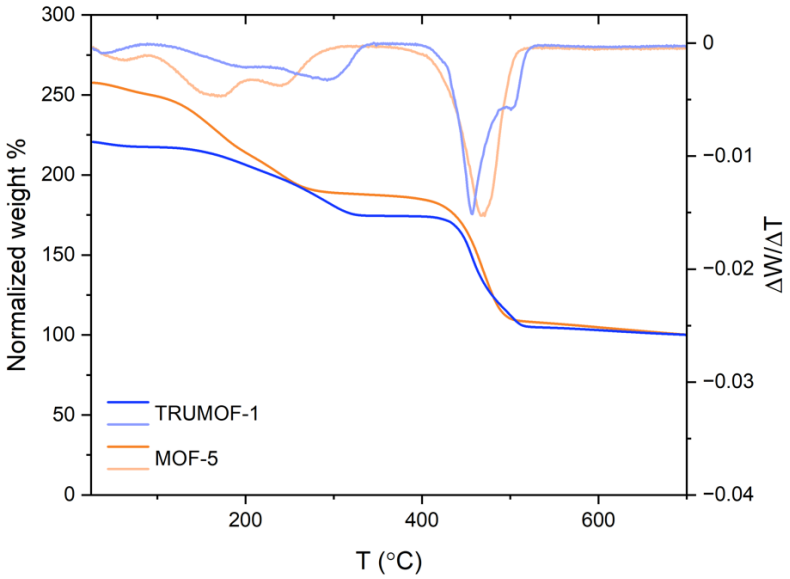

Fig. S4.

Thermogravimetric analysis measurements of TRUMOF-1 and MOF-5. The upper traces give the thermal derivative of the relative mass changes, which help identify the temperatures at which desorption/decomposition mechanisms switch.

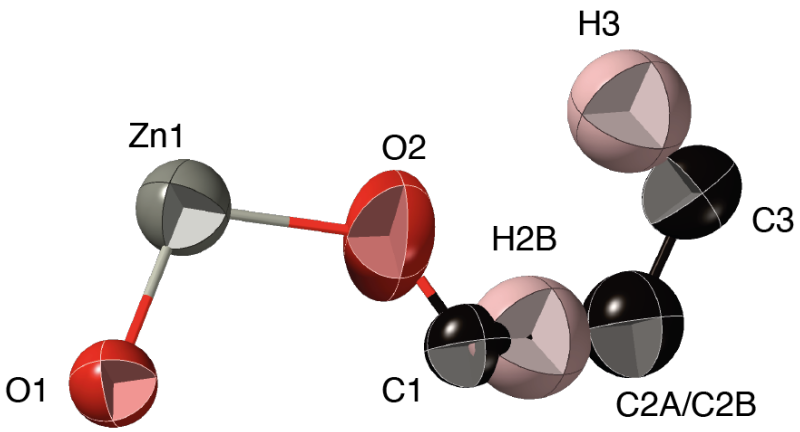

Fig. S5.

Representation of the asymmetric unit of our crystallographic model for the average structure of TRUMOF-1 at 100 K. Ellipsoids are drawn at 50% probability.

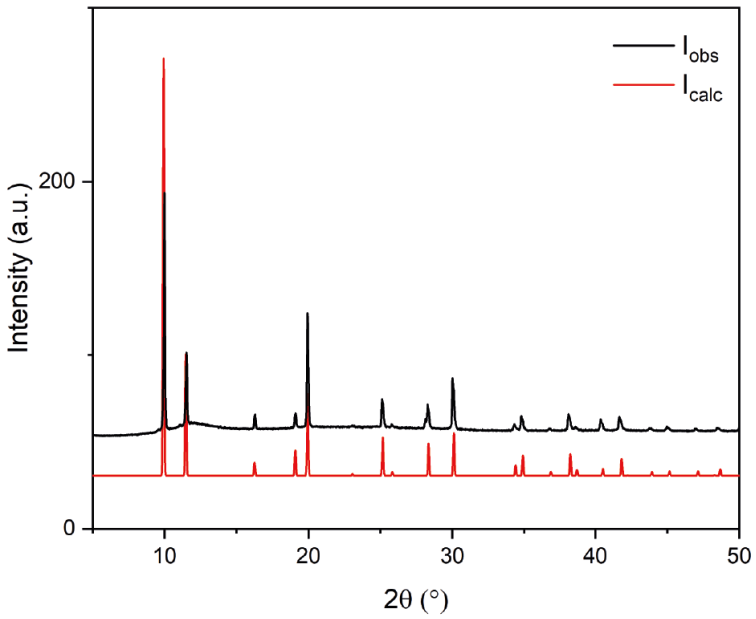

Fig. S6.

The experimental X-ray powder diffraction pattern (λ = 1.54 Å) at 300 K (black line) is well accounted for by the corresponding pattern calculated from our 300 K single-crystal X-ray diffraction solution (red line). Hence the single-crystal solution is representative of the bulk.

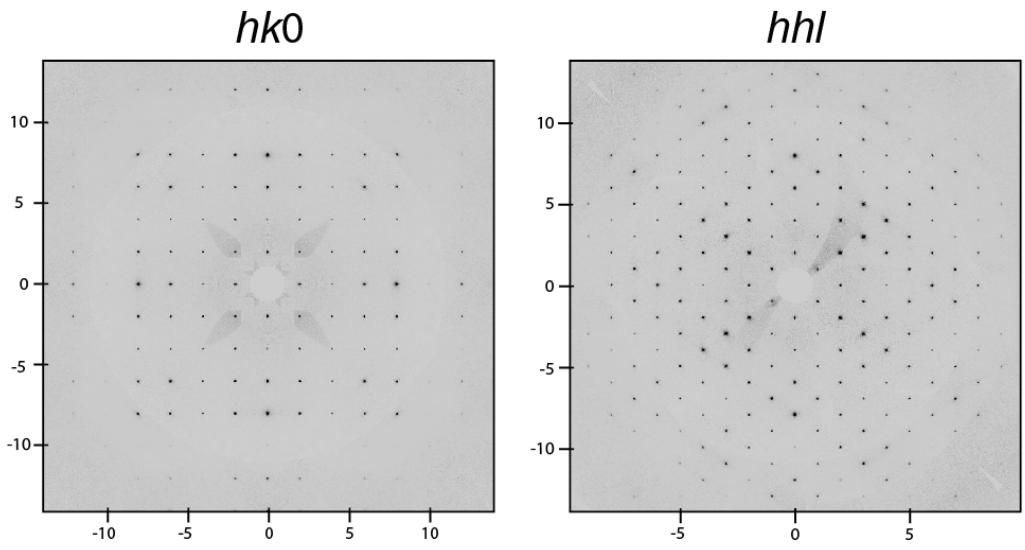

Fig. S7.

Reconstructed and symmetry averaged *hk*0 and *hhl* layers collected from TRUMOF-1 under Cu radiation at 300 K, collecting frames at an exposure time ranging from 0.45 to 2.82 seconds.

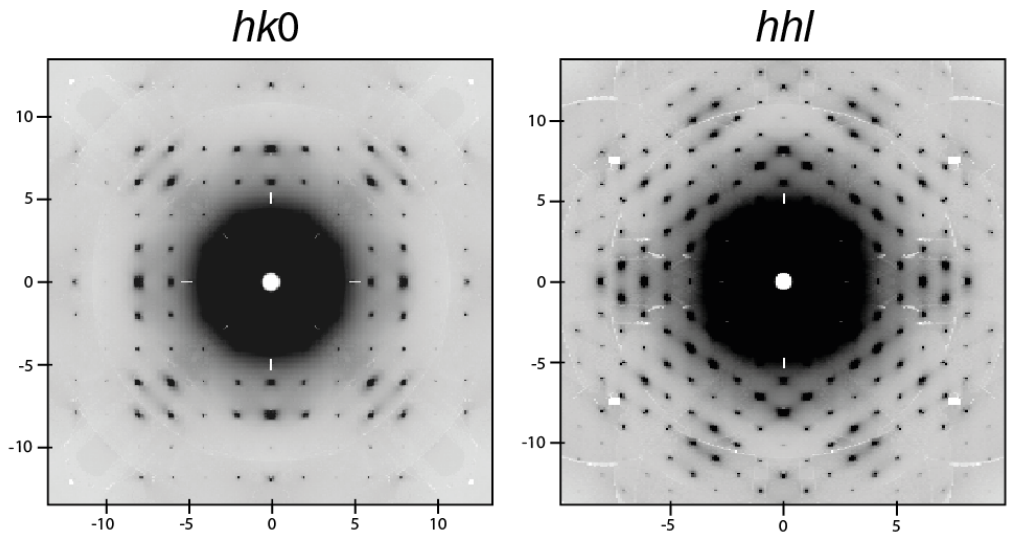

Fig. S8.

Reconstructed and symmetry averaged *hk*0 and *hhl* layers collected from TRUMOF-1 under Cu radiation at 300 K, collecting frames at an exposure time of 200 s.

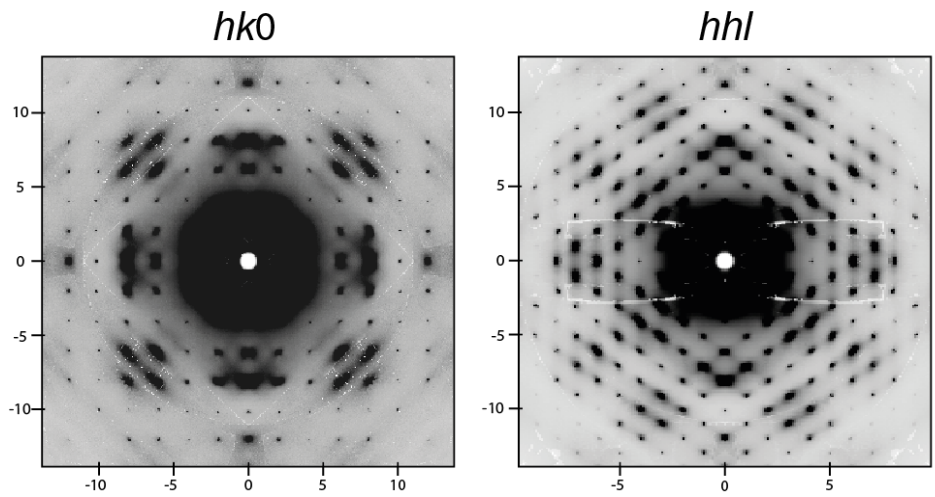

Fig. S9.
Reconstructed and symmetry averaged *hk*0 and *hhl* layers collected from iodine-soaked TRUMOF-1 under Cu radiation at 300 K, collecting frames at an exposure time of 200 s.

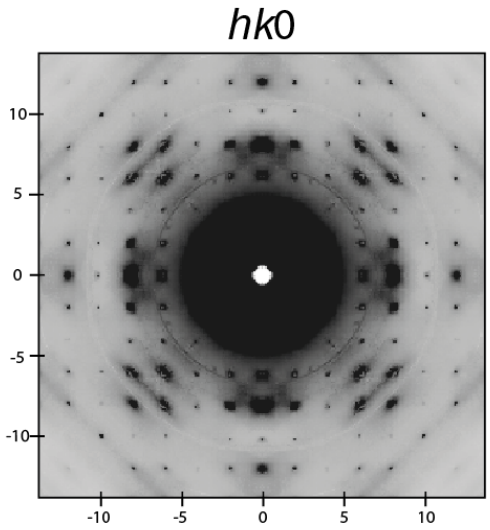

Fig. S10.

Reconstructed and symmetry averaged *hk*0 and layer collected from iodine-soaked TRUMOF-1 under Cu radiation at 120 K, collecting frames at an exposure time of 200 s. Note the diffuse ice ring around the origin.

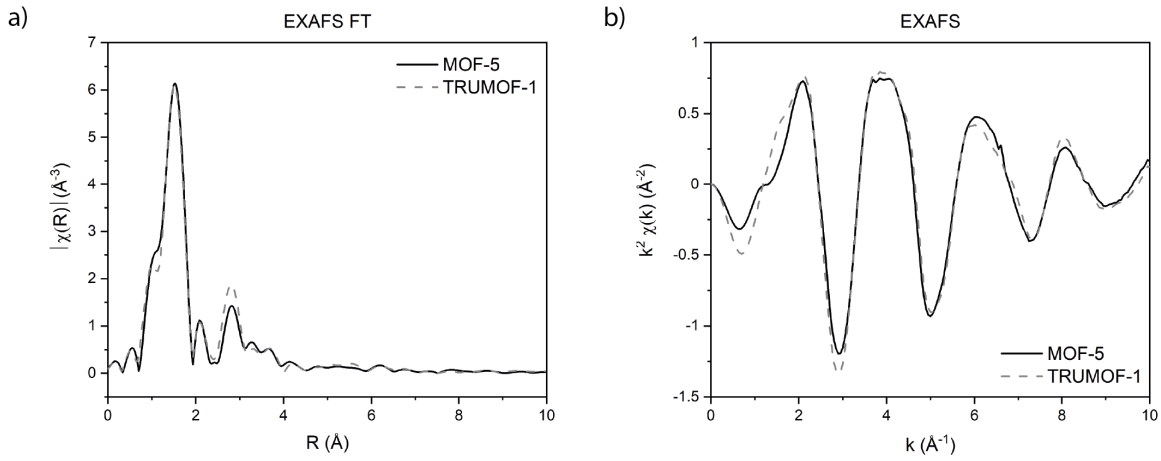

Fig. S11.

Zn K-edge EXAFS measurements and derived functions. (a) the real component of EXAFS Fourier transform shows similar features for both MOF-5 and TRUMOF-1. (b) The original EXAFS signal from which these Fourier transforms were obtained.

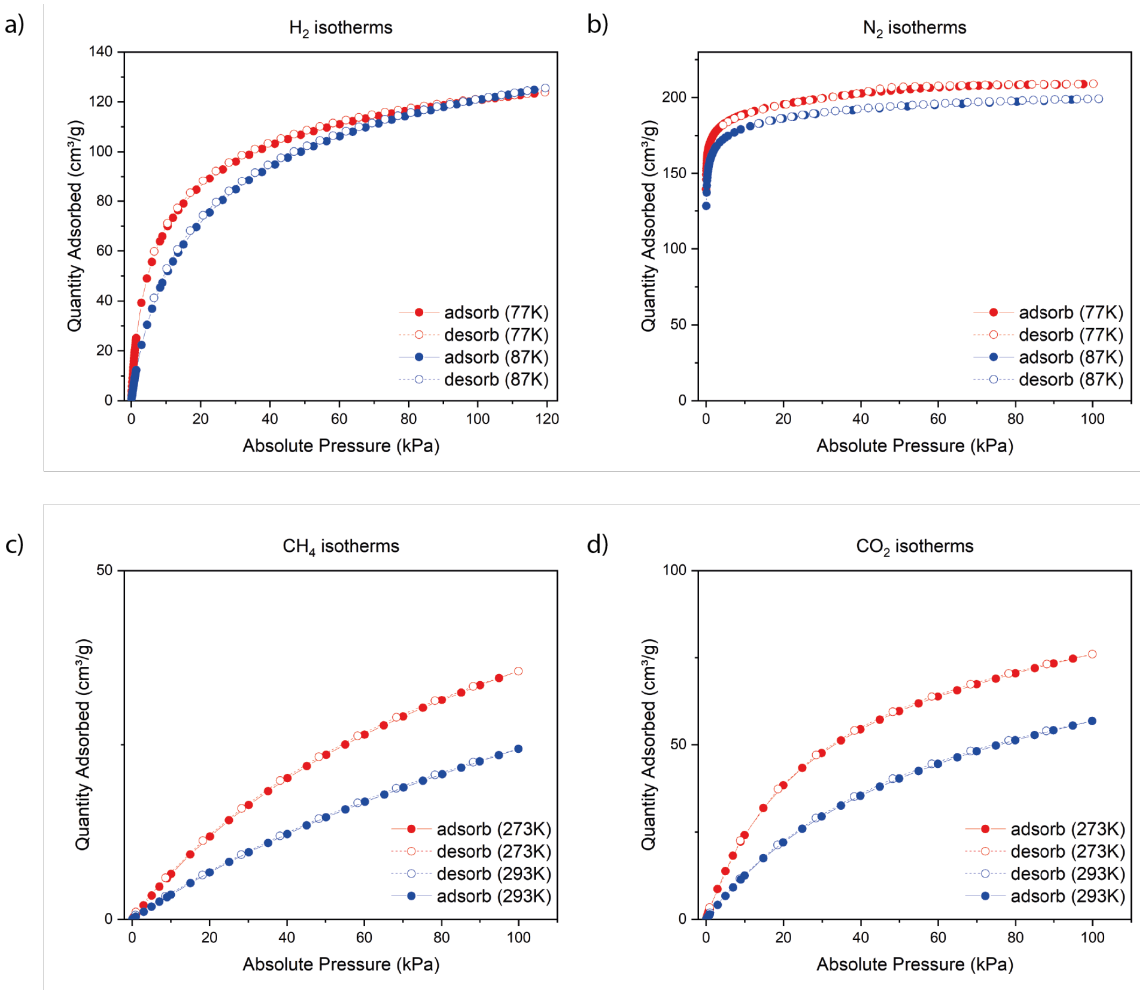

Fig. S12.

Adsorption and desorption isotherms of TRUMOF-1 with (a) H_2, (b) N_2, (c) CH_4 and (d) CO_2 gases at two different temperatures; quantities represent $cm^3\ g^{-1}$ uptake of each gas at standard temperature and pressure. The higher and lower temperature data are presented in blue and red, respectively.

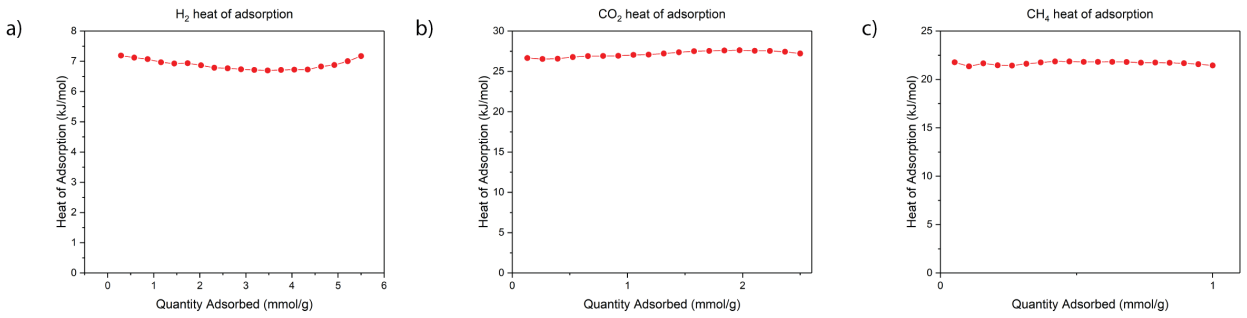

Fig. S13.

Heat of adsorption measurements of TRUMOF-1 with (a) H_2, (b) CO_2 and (c) CH_4 gases.

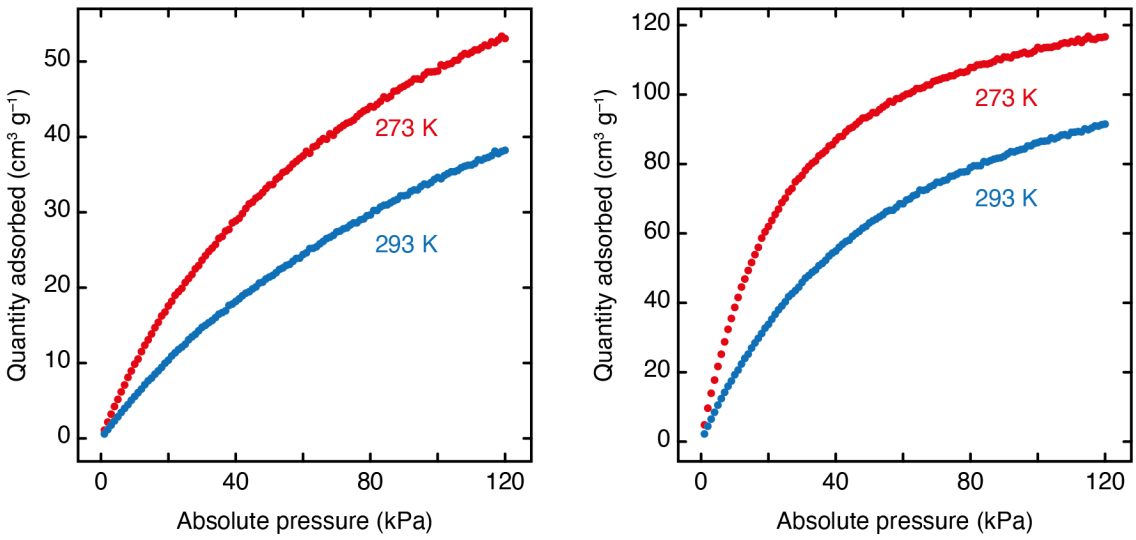

Fig. S14.

Adsorption isotherms of TRUMOF-1 for (left) CH_4 and (right) CO_2 calculated using GCMC simulations.

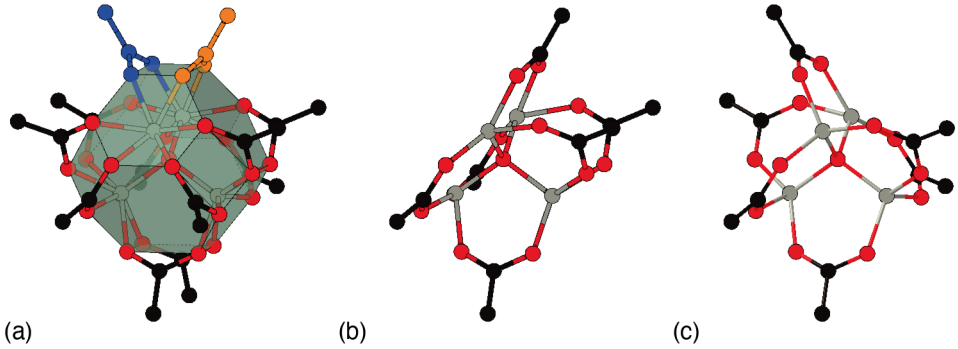

Fig. S15.

Determining cluster carboxylate occupancies in TRUMOF-1. (a) Each cluster site is surrounded by 12 partially-occupied carboxylate sites that partition into six pairs. These pairs are too close to one another to be occupied simultaneously; e.g. only one of the blue- and orange-coloured sites might be occupied at any one time. (b) Even within this constraint, some carboxylate decorations give unfeasibly distorted cluster geometries and so are excluded. (c) The decoration that disposes carboxylates as uniformly as possible.

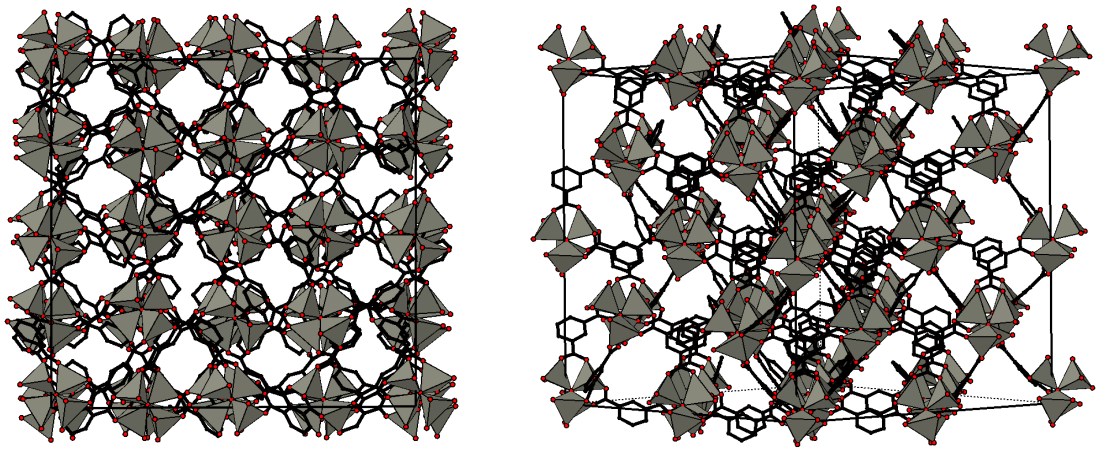

Fig. S16.

Representations of the geometry-optimised structure of one 2 × 2 × 2 TRUMOF-1 approximant, viewed down (left) [100] and (right) approximately [110] crystal axes. Zn coordination environments are shown as grey tetrahedra, and O and C atoms shown as red and black spheres, respectively.

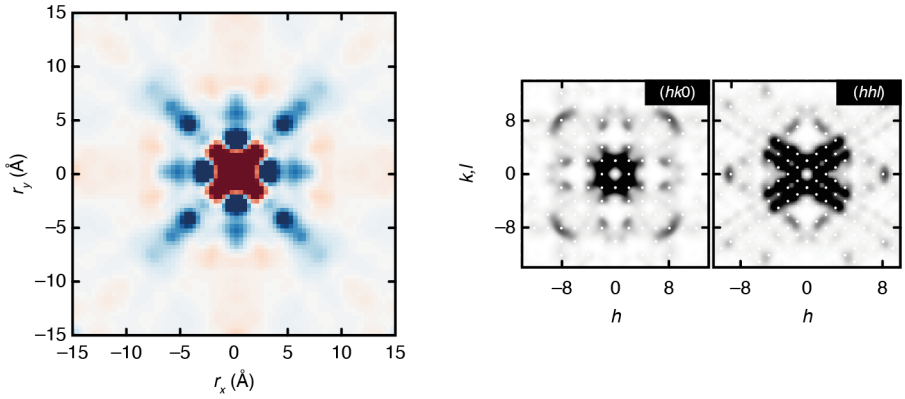

Fig. S17.

(Left) 3D-ΔPDF and (right) single-crystal diffuse scattering functions calculated for our Truchet-tile TRUMOF-1 models prior to geometry optimisation using DFT. The differences between these functions and those shown in Fig. 3 of the main text serve to highlight the experimental sensitivity to details of the TRUMOF-1 structure.

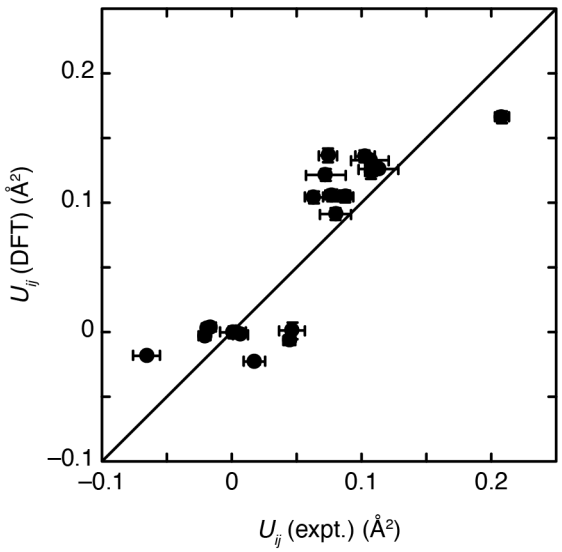

Fig. S18.

Contribution of static disorder to the anisotropic displacement parameters of TRUMOF-1 as determined using DFT, on the one hand, and estimated from linear fits to the experimental $U_{ij}(T)$ values, on the other hand. The observed values cluster around the diagonal.

Table S1.

Refined site occupancies in TRUMOF-1 obtained in the initial refinement step. The purpose of this refinement was to confirm the interpretation of ligand-site scattering density as reflecting an average over three orientations of 1,3-bdc molecules, each occupied with 25% likelihood. Uncertainties are omitted for constrained variables.

Atom	SOF	U_{iso} / Å^2	Wyckoff site	multiplicity	occupancy
Zn1	0.1667	0.0890(13)	16*e*	6	1
O1	0.0417	0.081(8)	4*a*	24	1
O2	0.46(3)	0.118(6)	96*i*	1	0.46(3)
C1	0.23	0.118	48*h*	2	0.46
C2	0.35(2)	0.118	48*h*	2	0.70(4)
C3	0.35	0.118	48*h*	2	0.70

Table S2.

Crystal data and structure refinement details for TRUMOF-1 at 100 K.

Empirical formula	$C_{24}H_{12}O_{13}Zn_4$
Formula weight / g mol^{-1}	769.82
Temperature / K	100.0(1)
Crystal system	cubic
Space group	$F\bar{4}3m$
a / Å	15.392(2)
V / Å^3	3646.3(16)
Z	4
ρ_{calc} / g cm^{-3}	1.402
μ / mm^{-1}	2.649
$F(000)$	1520.0
Crystal size / mm^3	0.16 × 0.125 × 0.05
Radiation	MoKα (λ = 0.710173 Å)
2θ range for data collection / º	4.584–51.338
Index ranges	$-14 \le h \le 18$, $-18 \le k \le 18$, $-18 \le l \le 17$
Reflections collected	6007
Independent reflections	392 [R_{int} = 0.1096, R_{sigma} = 0.0663]
Data/restraints/parameters	392/16/34
Goodness-of-fit on F^2	1.104
Final R indexes [$I \ge 2\sigma(I)$]	R_1 = 0.0615, wR_2 = 0.1569
Final R indexes [all data]	R_1 = 0.0766, wR_2 = 0.1794
Largest diff. peak/hole / e Å^{-3}	1.17/–0.51
Flack parameter	0.01(8)

Table S3.

Heat of adsorption (kJ mol^{-1}) of various gases in TRUMOF-1 (experimental) and MOF-5 (literature).

MOF	H_2	CO_2	CH_4
TRUMOF-1	7.2	26.7	21.8
MOF-5	3.8 (*62*)	–	12.6 (*63*)

Table S4.

Static-disorder contribution to the atomic displacement parameters extracted from the DFT-relaxed 2 × 2 × 2 approximants and estimated by extrapolation of the temperature-dependent U_{ij} values to 0 K.

Atom	Displacement parameter	DFT value (Å^2)	Experimental value (Å^2)
O1	U_{11}	0.104(5)	0.063(7)
Zn	U_{11}	0.105(5)	0.077(5)
	U_{12}	0.0000(2)	0.0035(9)
O2	U_{11}	0.104(4)	0.087(6)
	U_{22}	0.166(4)	0.208(5)
	U_{33}	0.124(5)	0.107(5)
	U_{23}	–0.002(2)	0.006(6)
	U_{13}	–0.0034(15)	–0.021(5)
	U_{12}	–0.0183(11)	–0.066(11)
C1	U_{11}	0.091(4)	0.080(12)
	U_{22}	0.121(4)	0.072(15)
	U_{23}	–0.023(2)	0.017(8)
	U_{13}	0.0027(12)	–0.019(3)
C2A/B	U_{11}	0.136(5)	0.074(7)
	U_{22}	0.133(4)	0.106(14)
	U_{23}	0.001(6)	0.046(9)
	U_{13}	0.004(4)	–0.017(4)
C3	U_{11}	0.136(5)	0.102(8)
	U_{33}	0.126(3)	0.113(15)
	U_{23}	–0.007(4)	0.044(5)
	U_{12}	0.000(5)	0.001(10)

Data File S1.

Temperature dependence of unit-cell parameters and atom coordinates in TRUMOF-1. Atom Wyckoff positions and coordinates as follows: O1 4*a* (0,0,0); Zn 16*e* (*x*,*x*,*x*); O2 96*i* (*x*,*y*,*z*); C1 48*h* (*x*,*y*,*y*); C2A/B 48*h* (*x*,*y*,*y*); H2B 48*h* (*x*,*y*,*y*); C3 48*h* (*x*,½–*x*,*z*); H3 48*h* (*x*,½–*x*,*z*).

Data File S2.

Temperature dependence of atomic displacement parameters for non-hydrogen atoms in TRUMOF-1.

Data File S3.

Geometry-optimised unit cell dimensions and relative energies for 1 × 1 × 1 TRUMOF-1 approximants.

Data File S4.

Geometry-optimised unit cell dimensions and relative energies for 2 × 2 × 2 TRUMOF-1 approximants.

Data File S5.

Crystallographic information files (.cifs) and checkcif reports for the experimental X-ray diffraction refinements of the average structure of TRUMOF-1 at 100, 140, 180, 220, 260, 300 and 340 K.

Data File S6.

Geometry-optimised structures for all ten 1 × 1 × 1 and twenty 2 × 2 × 2 TRUMOF-1 approximants.